Tong et al. *Zool. Res.* 2026, 47(6): 1907−1925
https://doi.org/10.24272/j.issn.2095-8137.2026.139
https://cstr.cn/32248.14.zr.2026.139

ZR | Zoological Research

Article Open Access

Repeated imiquimod challenge as an experimental model of psoriasiform inflammation and re-exposure associated reactivation

Xin Tong[1], Zhan Zhang[2,3], Zi-Hao Li[2,3], Cheng-Xin Li[1,*], Xu-Ming Zhou[2,*], Rui Wang[1,*]

[1] *Department of Dermatology*, *Chinese PLA General Hospital*, *Medical College of Chinese PLA*, *Beijing* 100853, *China*

[2] *Institute of Zoology*, *Chinese Academy of Sciences*, *Beijing* 100101, *China*

[3] *University of Chinese Academy of Sciences*, *Beijing* 100049, *China*

ABSTRACT

Long-term psoriasis management remains a major challenge worldwide. Although repeated imiquimod (IMQ) application has been used to mimic psoriatic inflammatory reactivation, it remains unclear whether this approach reflects amplified acute inflammation or the emergence of tissue-resident, memory-associated features. Here, we established a repeated IMQ-challenge model (IMQ-R) and compared it with a single-course IMQ model (IMQ-S) and human psoriatic lesions using bulk RNA sequencing (bulk RNA-seq) and single-cell RNA sequencing (single-cell RNA-seq). During the final induction phase, IMQ-R showed a more rapid re-emergence of skin inflammation than IMQ-S and displayed features of inflammatory reactivation in previously challenged skin, including IL-17-related pathways, TRM-related T-cell features, and predicted multicellular communication patterns. Single-cell analysis showed that IMQ-R exhibited a cellular composition more similar to active human psoriatic skin than IMQ-S, with keratinocyte (KC) expansion, endothelial cell (EC) enrichment, and relative preservation of T-cell populations. T-cell subsets with memory-associated annotations, including central memory T cells (TCM) and tissue-resident memory T cells (TRM), were increased in IMQ-R. In particular, IMQ-R was associated with enrichment of TRM17-related transcriptional features and enhanced predicted communication among T cells, keratinocytes (KCs), and myeloid cells, including IL-17-related signaling pathways. In summary, repeated IMQ challenge generates a psoriasiform model with accelerated inflammatory re-emergence and TRM-related features during re-exposure that are not fully captured by the conventional acute IMQ model. This model provides a useful platform for studying inflammatory reactivation after repeated challenge and for evaluating interventions targeting cutaneous memory-associated inflammatory programs.

Keywords: Psoriasis; Mouse model; Repeated IMQ challenge; Inflammatory reactivation; TRM17-like cells

INTRODUCTION

Psoriasis is a chronic, immune-mediated inflammatory skin disease characterized by recurrent erythematous, scaly lesions that frequently reappear at previously affected sites. Clinically, psoriasis relapse is usually defined by renewed worsening of disease after treatment withdrawal, such as loss of prior PASI improvement or an increase in Physician's Global Assessment (PGA) (Masson Regnault et al., 2022; Tian & Lai, 2022). However, these criteria reflect clinical outcomes rather than the underlying tissue immune state, and previously affected skin does not necessarily return to an immunologically normal baseline even after apparent clinical resolution, as resolved psoriatic lesions can retain a residual disease genomic profile (Suárez-Fariñas et al., 2011). Although biologic therapies targeting TNF, IL-23, and IL-17 have markedly improved disease control, inflammatory worsening commonly occurs after treatment withdrawal, suggesting that local tissue programs may persist within the skin and facilitate rapid reactivation upon secondary stimuli (Tian & Lai, 2022). Experimental and clinical studies indicate that re-emergence of psoriatic inflammation can involve multicellular tissue adaptation, in which pathogenic circuits arise from reciprocal signaling among dendritic cells (DCs), T cells, and keratinocytes (KCs), while stromal fibroblasts, endothelial cells, and mast cells create a permissive inflammatory niche that sustains and reactivates lesions (Francis et al., 2024; Li et al., 2024; Sieminska et al., 2024; Yao et al., 2025; Ye & Lai, 2025). Among these components,

This is an open-access article distributed under the terms of the Creative Commons Attribution Non-Commercial License (http://creativecommons.org/licenses/by-nc/4.0/), which permits unrestricted non-commercial use, distribution, and reproduction in any medium, provided the original work is properly cited.

Copyright ©2026 Editorial Office of Zoological Research, Kunming Institute of Zoology, Chinese Academy of Sciences

Received: 11 March 2026; Accepted: 25 May 2026; Online: 04 June 2026

Foundation items: This study was supported by the National Natural Science Foundation of China (82504266) and Institute of Zoology, Chinese Academy of Sciences (2023IOZ0104)

*Corresponding authors, E-mail: chengxinderm@163.com; zhouxuming@ioz.ac.cn; wr0699@163.com

tissue-resident memory T cells (TRM), particularly IL-17-producing TRM17 cells, have been implicated in disease persistence and lesion reappearance (Guo et al., 2023; Saavedra-Almarza et al., 2025). TRM17 cells have been detected in clinically resolved plaques, display heightened responsiveness to IL-23 signaling, and can rapidly produce IL-17A and IL-17F upon re-challenge. Their pathogenic activity is sustained through continuous interactions with KCs and DCs, mediated by cytokines, chemokines, and receptor–ligand networks such as the IL-23–IL-17 axis, CCL20–CCR6 signaling, and IL-1/IL-36-driven amplification loops (Yao et al., 2025; Ye & Lai, 2025).

The imiquimod (IMQ)–induced psoriasiform mouse (*Mus musculus*) model is widely used as it rapidly elicits epidermal hyperplasia, neutrophil and IL-17–driven inflammation, and a transcriptional profile that partially overlaps with human (*Homo sapiens*) psoriasis. However, conventional single-course IMQ application is generally thought to model an acute innate inflammatory response more closely than the full course of human plaque psoriasis. With prolonged treatment, the severity of IMQ-induced skin inflammation tends to plateau or partially attenuate, consistent with the engagement of endogenous counter-regulatory or resolution pathways in murine skin (Swindell et al., 2017; Tran et al., 2024). Thus, the standard single-course regimen has limitations for studying how previously inflamed skin responds to a subsequent inflammatory challenge (Madsen et al., 2018; Qiu et al., 2025). Recent studies have used repeated IMQ applications in BALB/c or C57BL/6 mice to induce more severe and persistent psoriatic dermatitis than single-phase induction (Fenix et al., 2020), highlighting the potential of recurrent IMQ exposure to examine selected features of inflammatory reactivation after prior challenge (Casciano et al., 2025; Chen et al., 2020; Deng et al., 2024a; Hu et al., 2025; Li et al., 2025; Saavedra-Almarza et al., 2025; Wu et al., 2025). Nonetheless, because tissue adaptation and T-cell residency are shaped by coordinated intercellular interactions, it remains unclear to what extent repeated IMQ challenge enriches TRM-related and IL-17-centered tissue programs compared with single exposure at the level of individual cell types. Thus, a systematic comparison of single-course versus repeated IMQ-induced inflammation, integrating both cellular composition and intercellular communication, has been lacking. From this perspective, sampling during the inflammatory phase after repeated IMQ challenge allows assessment of the active cellular programs that emerge after re-exposure.

In this study, we combined bulk RNA transcriptomic sequencing, single-cell transcriptomics and CellChat-based intercellular communication analyses in human psoriatic skin and two IMQ-based mouse models representing single and repeated inflammatory challenges. One was the conventional single-course IMQ model (IMQ-S), and the other was a repeated-challenge model (IMQ-R), in which mice were re-exposed to IMQ after visible recovery of the previously treated skin, with the aim of examining inflammatory reactivation after prior challenge. Focusing on T-cell memory-related annotations, psoriasis-relevant receptor programming, and cell communication patterns, we asked whether repeated IMQ challenge reveals inflammatory and TRM-related features that are less evident in the conventional acute model. Our results suggest that repeated IMQ challenge is associated with enrichment of TRM-related and IL-17-centered tissue programs during the final inflammatory phase, together with predicted broader stromal–immune interactions and may therefore serve as a useful experimental framework for studying repeated-challenge psoriasiform inflammation.

MATERIALS AND METHODS

Establishment of single-course and repeated-challenge IMQ-induced psoriasiform mouse models

All animal procedures were conducted in accordance with the ethical standards of the Institute of Zoology, Chinese Academy of Sciences, and were approved by its Laboratory Animal Ethics Committee (approval no. IOZ-IACUC-2024-079; March 5, 2024). Specific pathogen-free (SPF) male C57BL/6J mice (6–8 weeks old, 18–22 g) were obtained from Vital River Laboratory Animal Technology Co., Ltd. (China). Animals were maintained under controlled environmental conditions (25°C±2°C; 12 h light/dark cycle) with ad libitum access to standard chow and water.

Sample size was determined based on prior studies using IMQ-induced psoriasis-like models. Eighteen mice were randomly assigned to three groups (n=6 per group) using a random-number generator: IMQ-S group, IMQ-R group, and a control group (CTL).

Anesthesia was induced with 4%–5% isoflurane (Yipaining, China) and maintained with 1%–2% isoflurane in oxygen at a flow rate of 300–600 mL/min. Before treatment, a 2×2 cm area of dorsal skin was shaved to serve as a standardized application site. The treatment protocol consisted of induction and remission phases. During each induction cycle, 62.5 mg of 5% IMQ cream (Sichuan Medshine Pharmaceutical Co., China) or Vaseline (Aladdin, China) was topically applied to the dorsal skin of each mouse once daily for 5 consecutive days. During the remission intervals, mice received no treatment and were left undisturbed to allow spontaneous resolution of skin lesions, hair regrowth, and recovery of normal skin appearance. Mice in the IMQ-R group underwent three induction cycles separated by two remission intervals. In the IMQ-S group, mice received Vaseline rather than IMQ during the first two induction cycles and were treated with IMQ only during the final induction phase to control for cumulative handling and exposure history. Control mice received an equivalent amount of Vaseline during all induction periods.

During the final induction phase, body weight, dorsal skin thickness, and PASI scores were recorded daily (Jabeen et al., 2020). The PASI score was assessed based on erythema, scaling, and thickening of the dorsal skin, with each parameter graded on a scale of 0–4 and summed to yield a cumulative score ranging from 0 to 12. Scoring was performed in a blinded manner by investigators unaware of group allocation. At the experimental endpoint, mice were euthanized by CO_2 inhalation, and tissues (including dorsal skin and spleen) were harvested for subsequent analyses.

Hematoxylin and eosin (H&E) staining

Dorsal skin samples from the CTL, IMQ-S, and IMQ-R groups were collected and fixed in 4% paraformaldehyde (Solarbio, China) at room temperature for 24 h. Tissues were subsequently dehydrated through a graded ethanol series, cleared in xylene, and embedded in paraffin. Paraffin blocks were sectioned at 4–5 μm thickness using a rotary microtome.

Sections were deparaffinized in xylene and rehydrated through descending ethanol concentrations to distilled water. Hematoxylin and eosin (H&E) staining was performed

following standard protocols. Briefly, sections were stained with hematoxylin for nuclear visualization, rinsed in running tap water, differentiated in acid alcohol when required, and blued in alkaline solution. Sections were then counterstained with eosin to visualize cytoplasmic and extracellular matrix components, followed by graded dehydration, xylene clearing, and mounting with neutral resin.

To assess psoriasiform histopathology, epidermal thickness was measured as the vertical distance from the basal layer to the stratum corneum in at least five randomly selected, non-overlapping fields from one representative section per mouse using ImageJ software (NIH, USA). The mean value across the five fields for each mouse was used for statistical analysis. Histological evaluation and measurements were performed in a blinded manner by two independent investigators.

Immunohistochemistry

To assess the expression of the T-cell marker CD3 and the tissue-residency-associated marker CD103 in mouse skin lesions, tissue sections from each group were deparaffinized, rehydrated, and washed three times with PBS. Antigen retrieval was performed using heated Tris-EDTA buffer (Sigma-Aldrich, USA), followed by incubation with an endogenous peroxidase inhibitor. After blocking with 1% bovine serum albumin (BSA, Gibco, USA), the sections were incubated overnight at 4°C with a primary anti-CD103 antibody (1:3 000, Abcam, UK) or anti-CD3 antibody (1:3 000, Servicebio, China). The next day, sections were incubated with species-appropriate HRP-conjugated secondary antibodies (1:10 000, Abcam, UK) at room temperature, counterstained with hematoxylin, washed, dehydrated, cleared, and mounted.

For each group, six IHC-stained tissue sections were analyzed. From each section, five high-power fields (×20 magnification) were randomly selected and examined under a light microscope. The staining results were evaluated using a semi-quantitative scoring method by ImageJ software (Rueden et al., 2017).

Flow cytometry

For epidermal flow cytometry, mice were euthanized by carbon dioxide inhalation, and dorsal skin lesions (2×2 cm) were excised. After removal of subcutaneous tissue, skin samples were incubated with Dispase II (5 mg/mL; Yeason, China) at 37°C for 60 min. The epidermis was then gently separated and transferred into DNase I solution (100–150 μg/mL; Sigma-Aldrich, Germany) for further digestion at 37°C for 60 min to obtain single-cell suspensions. Digestion was terminated with RPMI-1640 medium containing 5% fetal bovine serum (FBS, Gibco, USA). Cell suspensions were filtered through a 70 μm cell strainer, centrifuged at 300 ×*g* for 5 min at 4°C, and resuspended in PBS containing 10% FBS.

For *ex vivo* stimulation, 20 mL of cell suspension was incubated with Cell Activation Cocktail with Brefeldin A (BioLegend, USA) at a dilution of 1:500, while an additional 10 mL of cell suspension was used as an unstimulated control. Cells were cultured at 37°C for 4 h, collected by centrifugation at 350 ×*g* for 5 min, and the supernatant was discarded. Cells were then resuspended in 2 mL Cell Staining Buffer (BioLegend, USA) and aliquoted into flow cytometry tubes at 100 μL per tube, with 1×10^6 cells per tube.

For Fc receptor blocking, cells were incubated with anti-CD16/32 antibody (1 μg per 1×10^6 cells; Multi Sciences Biotech, China) on ice for 15 min, followed by surface staining with fluorochrome-conjugated antibodies against CD45 (AF700), CD3 (PE-Cy7), CD8 (APC-Cy7), CD69 (FITC), CD103 (PE), and Zombie viability dye (PE-Texas Red) (1 μg/mL, all from BioLegend, USA) for 15 min at room temperature in the dark. For intracellular staining, cells were fixed and permeabilized using Fixation/Permeabilization buffer (eBioscience, China) according to the manufacturer's instructions and then stained with anti-IL-17A antibody (BV421, 1 μg/mL; BioLegend, USA) for 30 min on ice in the dark. After washing, cells were resuspended in PBS and analyzed on a BD FACS flow cytometer.

For skin flow-cytometry analysis, viable single cells were first selected, followed by CD45+ immune cells and CD3+ T cells. The resident memory-like T17 population was phenotypically defined as $CD45^+CD3^+CD69^+CD103^+IL\text{-}17A^+$ cells, and the $CD8^+$ TRM17-like population was defined within the $CD8^+$ T-cell gate as $CD45^+CD3^+CD8^+CD69^+CD103^+IL\text{-}17A^+$ cells. IL-17A-positive gates were interpreted relative to the IL-17A fluorescence-minus-one (FMO) controls (Supplementary Figure S1).

For spleen flow cytometry, spleens were mechanically dissociated and passed through a 70 μm cell strainer into 50 mL conical tubes, followed by red blood cell lysis using ACK lysis buffer (Solarbio, China). Cell suspensions were centrifuged at 300 ×*g* for 5 min at 4°C, and the cell pellets were resuspended in PBS containing 10% FBS. For Fc receptor blocking, cells were incubated with anti-CD16/32 antibody on ice for 15 min, followed by surface staining with fluorochrome-conjugated antibodies against CD45 (AF700), CLA (PE-Cy7), CD4 (BV605), CD8 (APC-Cy7), CD69 (FITC), CD103 (PE), KLRG1 (BV650), IL-7R (BV421), or 7-AAD (1 μg/mL, all from BioLegend, USA) for 15 min at room temperature in the dark. After washing, cells were resuspended in PBS and analyzed on a BD FACS flow cytometer (BD Biosciences, USA). Flow cytometry data were analyzed using FlowJo™ v.10.8 software (BD Life Sciences, USA).

RNA sequencing data acquisition and processing

Lesional skin from IMQ-R and CTL-R mice was homogenized in TRIzol (Thermo Fisher Scientific, USA), and total RNA was extracted using a mechanical tissue disruptor. Publicly available bulk RNA sequencing data of human psoriatic lesions and normal skin were downloaded from the Gene Expression Omnibus (GEO) database (for PP/NS, *n*=95/84, GSE54456). Bull RNA sequencing (Bulk RNA-seq) datasets of IMQ-S and corresponding control mouse skin (CTL-S) were obtained from GEO using the same criteria (*n*=4/per group, GSE86315).

RNA integrity was assessed using the Agilent 5300 Bioanalyzer. Samples with RNA integrity number (RIN) ≥7.0 were used for library preparation. mRNA was enriched using poly-A selection, followed by library construction using the Illumina Stranded mRNA Prep (Illumina, USA). RNA purification, reverse transcription, library construction and sequencing were performed at Shanghai Majorbio Bio-pharm Biotechnology Co., Ltd. (China) according to the manufacturer's instructions. Sequencing was performed on an Illumina NovaSeq 6000 platform with a paired-end 150 bp strategy.

Raw reads were processed for quality control, adapters and low-quality reads were removed using fastp (Chen, 2023). Clean reads were aligned to the mouse reference genome (GRCm38) using HISAT2 (Kim et al., 2019). The mapped

reads of each sample were assembled by StringTie (Pertea et al., 2015) in a reference-based approach. Transcript quantification was conducted using RSEM (Li & Dewey, 2011) on both gene and transcript levels. Differential gene expression analysis was performed using the voom function in the limma package (Ritchie et al., 2015) and DESeq2 (Love et al., 2014) packages after removing batch effects, with adjusted $P<0.05$ and $|\log_2(\text{fold change})|>1$ considered significant. Multiple testing correction was conducted using the Benjamini–Hochberg (BH) false discovery rate (FDR) method. Enrichment analyses of Kyoto Encyclopedia of Genes and Genomes (KEGG) pathways and Gene Ontology (GO) terms were conducted using ClusterProfiler (Yu et al., 2012).

Single cell preparation and sequence analysis

IMQ-R-treated and CTL-R group mouse skin samples were placed in sterile culture dishes containing 10 mL of 1×Dulbecco's Phosphate-Buffered Saline (DPBS, Thermo Fisher Scientific, USA) for transport. After discarding the residual buffer, tissues were minced into small fragments on ice. For enzymatic digestion, the samples were treated with a solution composed of 0.25% Trypsin (Thermo Fisher, USA) and 10 μg/mL DNase I prepared in PBS supplemented with 5% FBS. The digestion was performed at 37°C with gentle agitation (50 r.p.m.) for about 40 min. To optimize recovery and maintain cell integrity, the dissociated cells were harvested every 20 min during incubation. Afterward, the cell suspensions were passed through a 40 μm nylon mesh and washed with 1×DPBS containing 2% FBS. Cell viability was evaluated using 0.4% Trypan Blue (Thermo Fisher Scientific, USA), and viable cell counts were obtained using the Countess® II Automated Cell Counter (Thermo Fisher Scientific, USA).

Single-cell suspensions were then uniquely barcoded, and library construction was performed following the manufacturer's guidelines for the Chromium Single Cell 3′ v.3.1 kit (10x Genomics, USA). Sequencing was carried out on an Illumina NovaSeq 6000 platform using paired-end 150 bp reads (PE150).

Single cell RNA-seq data processing

Skin scRNA-seq datasets from human psoriasis and normal skin (for PP/NS, n=8/14, GSE173706), IMQ-S and CTL-S mouse skin (n=3/per group, GSE193350) were processed using the Seurat R package (v.5.4.0). Raw sequencing data were processed using the Cell Ranger software suite (v.7.1.0) (Zheng et al., 2017) with standard and manufacturer-recommended settings. FASTQ files obtained from Illumina sequencing were aligned to the mouse reference genome (GRCm38) through the STAR aligner (Dobin et al., 2013). Gene-barcode matrices were subsequently generated for each sample by counting unique molecular identifiers (UMIs) and filtering out barcodes not associated with genuine cells, resulting in a final matrix containing barcoded cells and their corresponding gene expression profiles.

Subsequent data processing and analysis were conducted in Seurat (v.5.4.0) (Satija et al., 2015). Quality control measures were applied to remove low-quality cells based on three established metrics: (1) total UMI count, (2) number of genes detected, and (3) mitochondrial gene percentage exceeding the mean±2 SD range. The mitochondrial read ratio was computed using Seurat's PercentageFeatureSet function (Satija et al., 2015).

Data normalization was performed with the NormalizeData function using the LogNormalize method, and highly variable features were identified while correcting for mean–variance dependency. All mouse model datasets were integrated into a single Seurat object through anchor-based integration using the RPCAIntegration method by the IntegrateLayers function with parameters "k.filter=30, k.weight=25" following the method described previously (Satija et al., 2015; Stuart et al., 2019) as correction for batch effect. Human datasets were also integrated using the same method. After scaling, the first 30 integrated RPCA components were retained for downstream steps. Cell clusters were visualized in two dimensions using uniform manifold approximation and projection (UMAP) (Healy & McInnes, 2024) and t-distributed stochastic neighbor embedding (t-SNE) (Van Der Maaten & Hinton, 2008).

Cells were grouped and further subclustered using graph-based clustering on integrated-RPCA-reduced dimensions via the Louvain algorithm (Blondel et al., 2008), following the generation of a shared nearest-neighbor (SNN) graph (Satija et al., 2015). Differentially expressed genes within each cluster were determined using the Wilcoxon rank-sum test compared to all other clusters. Cell type identity was assigned using SCINA (Aran et al., 2019) in conjunction with established marker gene references.

Differential expression analysis and Functional enrichment

Differentially expressed genes (DEGs) between two samples or clusters were identified using the FindAllMarkers function in Seurat with a likelihood ratio test. Genes with $|\log_2(\text{fold change})|>0.25$ and a Q value ≤0.05 were considered significantly differentially expressed, where Q values were obtained after multiple-testing correction using the BH-FDR method.

Sample-level cell-composition and sensitivity analyses

To evaluate cell-composition changes while preserving biological replication, cell-type proportions were calculated not only from pooled cells but also at the sample level. For the analysis of major cell populations, cells were grouped according to their sample identity, experimental group, and major or sub-cell-type annotation. The number of cells assigned to each major cell type was counted within each sample, and the corresponding proportion was calculated by dividing this count by the total number of cells recovered from that sample. Treatment-control differences were calculated within each model by comparing IMQ-S with CTL-S and IMQ-R with CTL-R.

To assess whether the observed compositional differences were influenced by unequal cell recovery across groups, equal-cell-number down-sampling was performed. In each iteration, the same number of cells was randomly sampled from each group, using the smallest group size among the compared groups as the reference. Major cell-type proportions were recalculated after down-sampling, and treatment-control fold changes were summarized across 100 iterations. To evaluate whether T-cell subpopulation patterns were robust to unequal T-cell recovery, the same down-sampling procedure was repeated within the T-cell compartment. Specifically, equal numbers of T cells were randomly sampled from each group, and the proportions of T-cell subclusters were recalculated relative to the total number of sampled T cells in each group.

Leave-one-sample-out sensitivity analysis was further

performed to examine whether the observed trends were driven by any individual biological sample. In each iteration, one sample was removed, and sample-level cell-type proportions were recalculated for the remaining samples. Treatment-control differences were then recomputed for major cell types. The same procedure was applied within the T-cell compartment to assess the robustness of T-cell subcluster proportion changes. These analyses were used as sensitivity assessments to determine whether the major compositional trends were retained after down-sampling or removal of individual samples.

CellChat analysis

To systematically characterize intercellular communication within the skin immune microenvironment, cell–cell interaction networks were inferred using the CellChat R package (v.1.6.1). Single-cell RNA sequencing data from PP/NS, IMQ-S/CTL-S, and IMQ-R/CTL-R were processed and analyzed separately.

A CellChat object was constructed for each dataset using normalized gene expression matrices. Known ligand–receptor interactions were retrieved from the CellChatDB database (Jin et al., 2025), including cytokine–cytokine receptor, chemokine, growth factor, extracellular matrix (ECM), and cell–cell contact signaling pathways. Communication probabilities between cell populations were computed using the default mass-action model implemented in CellChat, with expression thresholds applied to reduce noise from low-abundance genes.

Significant ligand–receptor interactions were identified by permutation testing (1 000 permutations), and only interactions with $P<0.05$ were retained for downstream analysis. The overall communication strength and number of interactions were quantified and compared across conditions. Pathway-level communication patterns were further analyzed by aggregating individual ligand–receptor pairs into curated signaling pathways.

To enable cross-condition comparison, communication networks from human psoriasis, IMQ-S, and IMQ-R datasets were jointly analyzed using the mergeCellChat function. Differences in interaction strength, signaling pathway activity, and sender–receiver roles among major cell types were visualized using heatmaps, circle plots, and network diagrams.

Pseudotime Analysis

Pseudotime trajectory analysis was performed using the Monocle3 package (v.1.4.26) (Cao et al., 2019). Processed Seurat objects were directly converted into Monocle3 cell_data_set objects using the SeuratWrappers interface, allowing preservation of previously curated metadata, cell-type annotations, and dimensionality reduction results. To ensure consistency between clustering and trajectory inference, the UMAP embeddings generated in Seurat were imported and used as the reduced dimensional space for Monocle3 analyses rather than recalculating dimensionality reduction.

Cells were ordered along trajectories using the learn_graph and order_cells functions with default parameters. The root of the trajectory was defined based on biologically inferred starting populations representing the least differentiated or baseline cell state, enabling reconstruction of dynamic transitions associated with disease progression. No additional batch correction or re-clustering was applied during Monocle3 processing to avoid introducing structure inconsistent with the original Seurat analysis.

Genes exhibiting dynamic expression along pseudotime were identified using graph-based Moran's I testing implemented in Monocle3. Significant genes were subsequently visualized as expression trends across pseudotime. For clearer interpretation of lineage-associated transcriptional programs, selected gene sets were plotted as smoothed expression heatmaps and KEGG pathway enrichment was conducted using the ClusterGVis package (Zhang et al., 2026), which enabled hierarchical clustering of genes according to their temporal expression patterns. This workflow ensured that trajectory inference represented a direct extension of the Seurat-derived cellular landscape while enabling identification of temporal transcriptional changes associated with cellular state transitions.

Statistical analysis

All statistical analyses were performed using GraphPad Prism v.10.0.0 (www.graphpad.com). Continuous variables were assessed for normality using the Shapiro-Wilk test. Variables with a normal distribution were presented as mean±standard deviation (SD), while non-normally distributed variables were expressed as median and interquartile range (IQR). For comparisons among multiple groups, one-way analysis of variance (ANOVA) was employed for normally distributed data with homogeneity of variances, followed by Bonferroni post hoc tests for pairwise comparisons. For non-normally distributed data or when the assumption of homogeneity of variances was violated, the Kruskal-Wallis test was used, followed by Dunn's test with Bonferroni correction for multiple comparisons. Categorical variables were compared using the Chi-square test. A P-value of <0.05 was considered statistically significant.

RESULTS

IMQ-R induces a more rapid-onset psoriasiform dermatitis than IMQ-S without evidence of greater body-weight loss

To compare the phenotypic characteristics of the multi-stage, repeated IMQ stimulation protocol with a conventional single-stage IMQ model of psoriasiform dermatitis, mice were subjected to either IMQ-S or IMQ-R treatment (Figure 1A). During the final induction phase, body weight was monitored longitudinally, and disease severity was systematically assessed using PASI scores and lesion thickness measurements. Gross observation and histological examination further showed that visible lesions largely resolved, and the skin architecture had largely returned to a near-normal state during the interval periods before the final re-challenge (Supplementary Figure S2). Macroscopic assessment indicated that, relative to IMQ-S, the IMQ-R model exhibited a more rapid onset and greater persistence of inflammation during the final induction. Specifically, IMQ-R-treated mice developed evident erythema, scaling, and skin thickening as early as two days (Day 50) after the start of the final induction, with inflammation peaking on the third day (Day 51) and remaining at a high level thereafter. By contrast, IMQ-S-treated mice showed more apparent psoriasiform features from the third day, with peak severity occurring on the fifth day (Day 53, Figure 1B).

Histopathological analysis was performed on lesional skin collected at the end of the final induction. Both IMQ-S and IMQ-R groups displayed classic psoriasiform features compared with controls, including marked epidermal thickening with pronounced acanthosis, hyperkeratosis, and

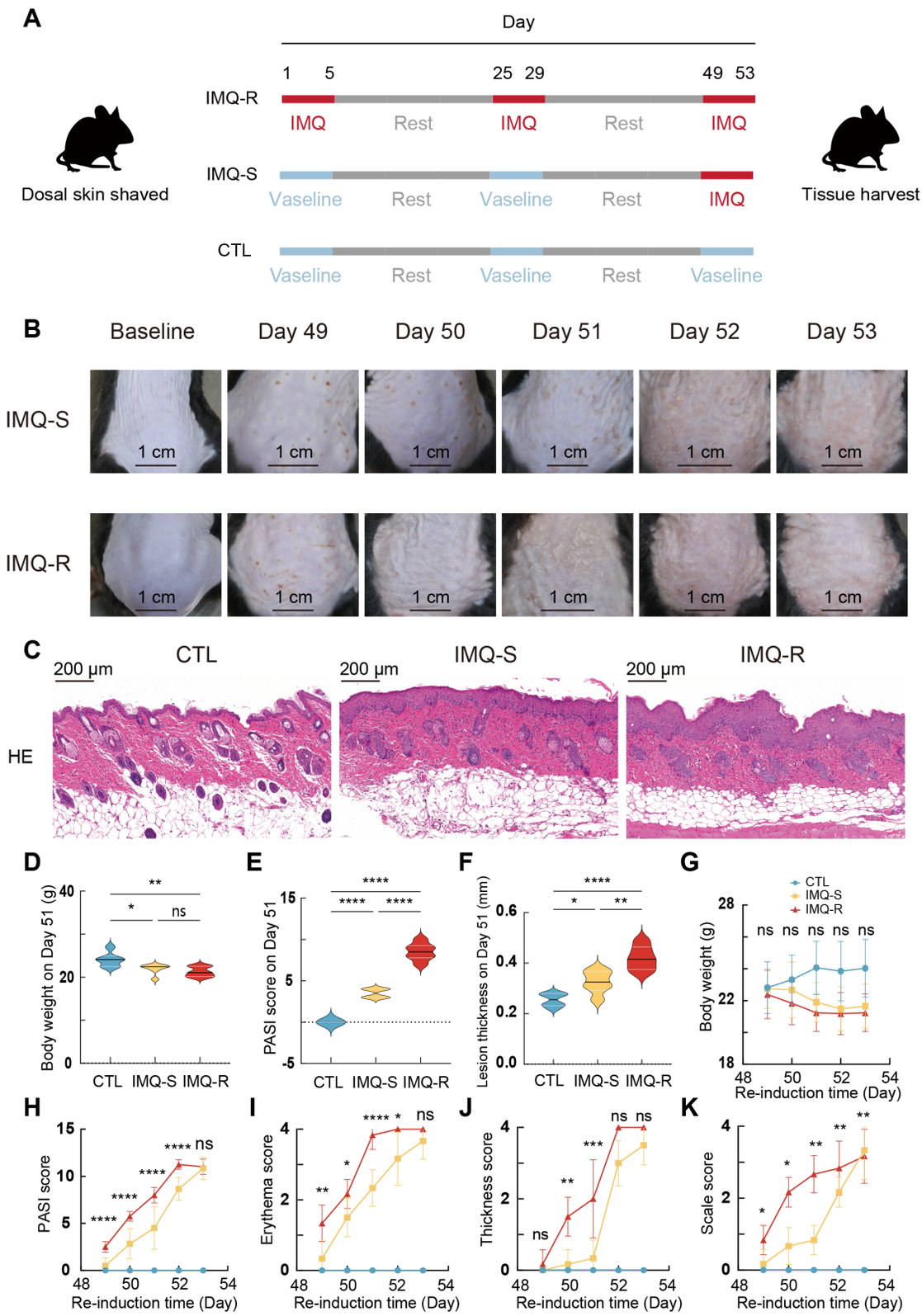


Figure 1 Pathological characterization of IMQ-S and IMQ-R psoriasis-like mouse models

A: The *in vivo* experiment design of IMQ-S and IMQ-R psoriasis-like mouse model. B: Representative photographs (by Xin Tong) of dorsal skin from IMQ-S and IMQ-R mice at the end of the final induction phase (Scale bar: 1 cm). C: Hematoxylin and eosin (H&E)–stained sections of skin from the CTL, IMQ-S, and IMQ-R groups (Scale bar: 200 μm). D–F: Distribution of body weight (D), PASI score (E), and lesion thickness (F) in Control, IMQ-S, and IMQ-R mice on day 51. G–K: Daily changes in disease-related parameters during the final induction phase in CTL, IMQ-S, and IMQ-R groups, including body weight (G), PASI score (H), erythema score (I), thickness score (J), and scaling score (K). Significance between IMQ-S and IMQ-R at each time point, as shown in the figure, was determined by Holm-adjusted post hoc comparisons following repeated-measures analysis. CTL: Control group; IMQ-S: Single-course IMQ model; IMQ-R: Repeated IMQ-challenge model. ns: Not significant; *: P<0.05; **: P<0.01; ***: P<0.001; ****: P<0.0001.

dense inflammatory infiltration. These changes appeared more pronounced in IMQ-R than in IMQ-S lesions (Figure 1C), consistent with more rapid inflammatory re-emergence under repeated challenge conditions.

Consistent with the histological findings, PASI scores and lesion thickness in both IMQ-S and IMQ-R groups were significantly higher than those in controls throughout the final induction, whereas body-weight changes did not differ significantly between the two IMQ-treated groups (Figure 1D–K). On the third day, both indices were significantly greater in IMQ-R than in IMQ-S (Figure 1E, F; IMQ-S vs. IMQ-R, PASI: 3.50±0.55 vs. 8.50±1.05, P<0.0001; thickness: 0.33±0.04 mm vs. 0.42±0.05 mm, P<0.0001). With continued stimulation, disease severity in IMQ-S increased and the differences between the two models became less pronounced; by the fifth day, PASI scores were largely comparable (Figure 1H–K). These findings suggest that the aggravated cutaneous inflammation observed in IMQ-R primarily reflects rapid local immune activation rather than increased systemic drug burden or generalized stress, a property that may be useful for studying inflammatory re-emergence after repeated challenge.

Comparative transcriptomic analysis of IMQ-R or IMQ-S models in relation to chronic human psoriasis

Although clinical and histological assessments indicated that IMQ-R elicits a faster local inflammation than IMQ-S, whether their immunological mechanisms differed remained unclear. We therefore performed bulk RNA-seq to compare molecular features of IMQ-S and IMQ-R skin lesions and to evaluate their similarity to human disease. Lesional skin from IMQ-R-treated mice and matched controls (CTL-R; n=6/6) was sequenced *de novo*. Since the IMQ-S protocol included an additional depilation/interval step that could confound transcriptional output, conventional IMQ datasets (IMQ-S/CTL-S; n=4/4) were obtained from public repositories. For cross-species comparison, transcriptomic data from human psoriasis (PP) and normal skin (NS) were also included (n=95/84). All datasets were reprocessed through a unified pipeline to minimize bioinformatic bias, and the focus was placed on fold change (FC) rather than absolute expression levels. Using an adjusted P<0.05 and $|\log_2(\text{fold change})|$>1, we identified 3 434 differentially expressed genes (DEGs) in PP vs. NS (1 576 upregulated, 1 858 downregulated), 2 281 in IMQ-S vs. CTL-S (976 up, 1 305 down), and 1 746 in IMQ-R/CTL-R (831 up, 915 down, Figure 2A–C).

Integration of GeneCards, OMIM, and TTD yielded a psoriasis-related gene set of 3 578 genes. Intersection with PP vs. NS DEGs produced 512 psoriasis-associated DEGs (346 up, 166 down), which can be mapped to murine homologues (Supplementary Figure S3A). Among the top upregulated human psoriasis genes were *S100A9, S100A8, AKR1B10, SERPINB4, GJB2, IL36G,* and *FABP5*. Within this curated psoriasis gene set, IMQ-S lesions identified 430 psoriasis-related DEGs (237 up, 193 down), whereas IMQ-R identified 322 (216 up, 106 down). Notably, four of the top IMQ-R genes (*S100a8, S100a9, Serpinb3, Fabp5*) overlapped with human psoriasis, compared with only one in the IMQ-S model (*Serpinb3*).

Despite the smaller number of total DEGs, transcriptional changes in IMQ-R captured more features of core human psoriatic signatures. Correlation analysis of the top 50 psoriasis genes showed a stronger concordance between IMQ-R and human PP (Spearman R=0.66) than between IMQ-S and PP (R=0.58), and this pattern was maintained when the top 100 and 150 genes were examined (Figure 2D; Supplementary Figure S3B, C). Key inflammatory cytokines implicated in psoriasis pathogenesis, including *Il36a, Il36g, Il17a, Il17f,* and *Il20,* were more strongly induced in IMQ-R lesions, whereas IMQ-S lesions preferentially reflected suppression of homeostatic genes such as *Il34* and structural transcripts (*Tnnt2, Tnnt3*; Figure 2E).

At the pathway level, IMQ-R also appeared to be more comparable to human psoriasis than IMQ-S (Supplementary Figure S4A, B). GO terms enriched in psoriatic lesions were likewise enriched in the IMQ-R model, with higher rich factors and stronger statistical significance than in the IMQ-S model (Supplementary Figure S4A). IMQ-R recapitulated all of the top ten KEGG pathways enriched in human psoriasis, whereas IMQ-S captured eight of these pathways (Supplementary Figure S4B). Gene set enrichment analysis using Gene Ontology (GSEA-GO) further showed a broader functional overlap between IMQ-R lesions and human psoriasis, including enrichment of immune-defense related processes (e.g., response to bacterium/organism/symbiont), while IMQ-S lesions shared a more limited overlap with these immune-response pathways (Supplementary Figure S4C–E).

Together, transcriptomic, gene-level, correlation, and pathway analyses indicated that IMQ-R may more closely reproduce selected molecular features of active human psoriatic lesions and the rapid inflammatory re-emergence observed during re-exposure, whereas IMQ-S induces a broader but less disease-specific inflammatory program.

Single-cell profiling reveals distinct cellular compositions in IMQ-S and IMQ-R models relative to human psoriasis

Although bulk transcriptomic analyses showed that IMQ-R exhibited greater concordance with human psoriatic lesions than IMQ-S at the global level, the corresponding single-cell immune landscape of IMQ-R remained unclear. To characterize the local cellular microenvironment in greater detail, we performed single-cell RNA sequencing (scRNA-seq) and compared IMQ-R with IMQ-S and human psoriasis datasets. scRNA-seq was conducted on dorsal skin from CTL-R and IMQ-R mice (IMQ-R/CTL-R, n=3/3). Publicly available datasets were incorporated for comparison: including IMQ-S/CTL-S mouse samples (n=3/3) and human psoriatic lesions (PP), and normal skin (NS) (n=14/8). After stringent quality control and data integration, a total of 160 208 cells were retained for analysis (PP: 36 886; NS: 11 584; IMQ-S: 31 566; CTL-S: 26 999; IMQ-R 15 010; CTL-R 38 163; Supplementary Figure S5, S6). All datasets were processed using a unified analytical workflow, and disease-associated differences were evaluated based on proportional and fold changes rather than absolute counts to minimize potential bias related to sequencing-depth. Annotation using canonical markers by SCINA identified five major cell types in human skin—endothelial cells (ECs), fibroblasts (FCs), myeloid cells, T cells, and KCs (Supplementary Figure S5A, B, E, F; Supplementary Figure S6A, B). Mouse skin contained an additional myocyte population, yielding six cell types overall (Supplementary Figure S5C, D; Supplementary Figure S6C, D).

In human psoriasis, KCs predominated (69.39%), followed by FCs (14.59%), T cells (7.25%), ECs (6.18%), and myeloid cells (2.59%). IMQ-S showed a markedly different composition

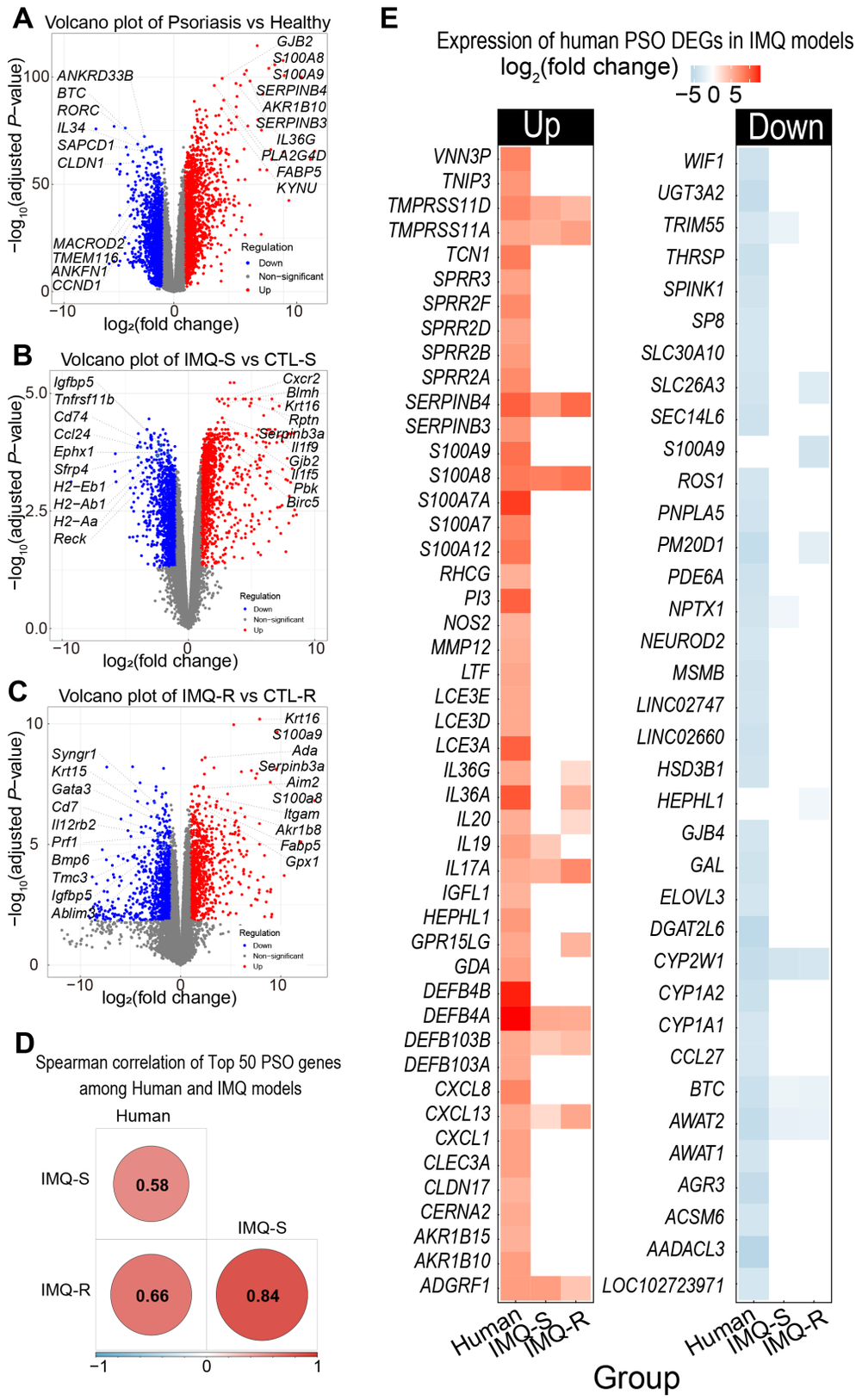


Figure 2 Global transcriptomic profiling of psoriasis patients, IMQ-S, and IMQ-R mouse models

A–C: Volcano plots of differentially expressed genes (DEGs) in psoriasis patients versus healthy controls (A), the IMQ-S model versus its control group (B), and the IMQ-R model versus its control group (C). Significantly upregulated and downregulated genes are shown in red and blue, respectively, while non-significant genes are shown in gray. The top 20 genes with the greatest fold changes and known relevance to psoriasis are labeled on both sides. D: Spearman correlation heatmap of the top 50 highly expressed psoriasis-related genes across psoriasis patients and the IMQ-S and IMQ-R models. Circle size and color indicate the magnitude of the correlation coefficient; all correlation test P<0.05. E: Heatmap showing expression changes of the top 50 DEGs from psoriasis patients across patient samples, IMQ-S, and IMQ-R models, with upregulated genes in red and downregulated genes in blue. CTL: Control group; IMQ-S: Single-course IMQ model; IMQ-R: Repeated IMQ-challenge model.

dominated by myeloid cells (36.40%) and FCs (30.77%), with reduced KCs (25.84%). In contrast, IMQ-R closely mirrored human lesions, with KCs again dominant (69.57%), followed by myeloid cells (25.41%) and preserved T-cell, FCs, ECs, and myocyte populations (Supplementary Figure S5G and sample-level cell counts are presented in Supplementary Table S1). Fold-change analysis further underscored these distinctions. In PP versus NS, myeloid cells increased most prominently (3.30-fold), followed by ECs (2.56-fold), T cells (1.85-fold), and FCs (1.24-fold), whereas KCs were modestly reduced in relative terms (0.85-fold). In the IMQ-S model, disease-associated changes were dominated by expansion of FCs (1.65-fold) and myeloid cells (1.57-fold), accompanied by marked relative decreases in KCs (0.58-fold) and T cells (0.53-fold). By contrast, IMQ-R lesions demonstrated increased proportions of ECs (2.22-fold), FCs (1.42-fold), KCs (1.36-fold), and T cells (1.05-fold), with a relative decrease in myeloid cells (0.57-fold). We also conducted down-sampling and leave-one-sample-out analyses; these different trends of cell composition variation in IMQ-S and IMQ-R models remain regardless of the sample sizes or specific samples (Supplementary Figures S7, S8).

Thus, although both models reproduced fibroblast expansion, their immune architectures differed fundamentally: IMQ-S reflected an acute, innate immune–dominant inflammation marked by broad myeloid accumulation, whereas IMQ-R exhibited KCs expansion, ECs enrichment, and preserved T-cell participation, more consistent with the epidermal hyperplasia, superficial vascular remodeling, and sustained adaptive immunity seen clinically. Notably, the lower myeloid-cell increase observed in IMQ-R does not necessarily indicate attenuated inflammation. Instead, it may suggest that repeated challenge shifts the inflammatory response away from one predominantly characterized by marked myeloid recruitment and toward a tissue context shaped by previous inflammatory exposure. This does not imply that innate immunity is no longer important in IMQ-R; rather, it indicates that the repeated-challenge model may combine innate activation with re-engagement of local tissue programs generated by prior challenge. Multiple, non-mutually exclusive mechanisms may underlie this difference, although these possibilities remain to be functionally tested (Supplementary Figure S5H).

IMQ-R expands the proportion of long-memory T cells and faithfully recapitulates human inflammatory and stress-related transcriptional programs

Given that KCs, myeloid cells, and T cells have been implicated as key mediators of inflammatory re-emergence in previously affected psoriatic skin (Sieminska et al., 2024; Swindell et al., 2013), subsequent analyses were undertaken to examine the profiles of these populations. We first compared T-cell composition and function between IMQ-S and IMQ-R. After stringent quality-control filtering, 6 614 T cells were analyzed (NS 439; PP 2 886; CTL-S 1 354; IMQ-S 835; CTL-R 933; IMQ-R 385). Using a machine learning–assisted annotation framework, human and mouse T cells were classified according to their transcriptional programs into six subsets: naïve T cells (Tn), NK T cells, central memory T cells (TCM), effector memory T cells (TEM), regulatory T cells (Treg), and TRM (Figure 3A–D; Supplementary Figure S9; the sample-level cell counts are presented in Supplementary Table S2).

Relative to normal skin, human psoriatic lesions showed that strongest expansion of NKT cells (10.18-fold), followed by TCM (5.81-fold), Treg (5.50-fold), TEM (1.31-fold), and TRM (1.27-fold). By contrast, IMQ-S did not exhibit clear expansion of any T-cell subset and instead showed mild relative reductions across populations, consistent with an acute inflammatory response with limited enrichment of memory-annotated T-cell states. However, IMQ-R, demonstrated enrichment of T-cell subsets annotated with memory-related programs, with TCM increasing 6.29-fold, TRM 2.64-fold, and Treg 1.41-fold, suggesting that repeated challenge is associated with a stronger representation of these T-cell states during final re-exposure (Supplementary Figure S10A). This trend was also consistently observed in iterative down-sampling and leave-one-sample-out analyses except for Treg-like subpopulations in the leave-one-sample-out analysis, which showed fewer stable changes and were therefore not emphasized as a reliable conclusion in the present study (Supplementary Figures S11, S12). Consistent with this increase in memory-annotated and regulatory populations, IMQ-R more robustly engaged psoriasis-defining inflammatory signaling than IMQ-S with greater induction of TNF/IL-23/IL-17–axis genes, including *Il23r, Il21r, Ccr6, Il17a*, and *Il17f* (Supplementary Figure S10B).

To further evaluate how faithfully IMQ-S and IMQ-R reproduce human KC pathology, we compared KC subset composition and inflammatory transcriptional programs among psoriasis patients, IMQ-S, and IMQ-R. UMAP analysis identified highly conserved KC populations across species—basal, cycling, hair follicle–associated, spinous, and wound/stress-associated KCs (Figure 4A, B; Supplementary Figures S13, S14). However, their proportional distributions differed markedly between conditions (Figure 4C), indicating distinct epidermal response patterns. Both IMQ models showed strong expansion of wound/stress-associated and spinous KCs, consistent with IMQ-induced epidermal stress and abnormal differentiation, yet this effect was substantially greater in IMQ-R: these populations increased 1 130.30-fold in IMQ-S versus 1 823.61-fold in IMQ-R (Figure 4D).

Gene-level comparison further supports a closer molecular alignment between IMQ-R and human psoriasis (Figure 4E). Psoriatic KCs displayed a canonical inflammatory program marked by upregulation of cytokine/chemokine genes (CCL20, DEFB4A/GSEA1, CXCL8, IL1B and IL36G), activation of stress-signaling mediators (e.g., NFKBIA and MAPK-pathway genes), and increased expression of metabolic/solute transport regulators (SLC family). Core inflammatory amplifiers (S100a7a/S100a7b, Krt16, Il36rn) were shared among IMQ-S, IMQ-R, and human lesions; notably, several IL-1/IL-36-axis genes (*Il1b, Il1r1 and Il1rn*) showed stronger concordance between IMQ-R and human psoriasis, supporting a closer association of IMQ-R with keratinocyte inflammatory amplification and repeated-challenge tissue programs.

At the same time, IMQ-S showed relatively stronger acute chemokine/interferon-oriented features, with prominent induction of *Ccl20, Cxcl1, Cxcl2, Cxcl10*, and interferon-response genes such as *Ifngr1, Ifngr2*, and *Stat1*. Importantly, this pattern suggests that IMQ-S may better capture selected aspects of early innate inflammatory activation and chemokine-driven recruitment, highlighting that the two models differ in emphasis rather than showing a consistent advantage of one over the other across all molecular features.

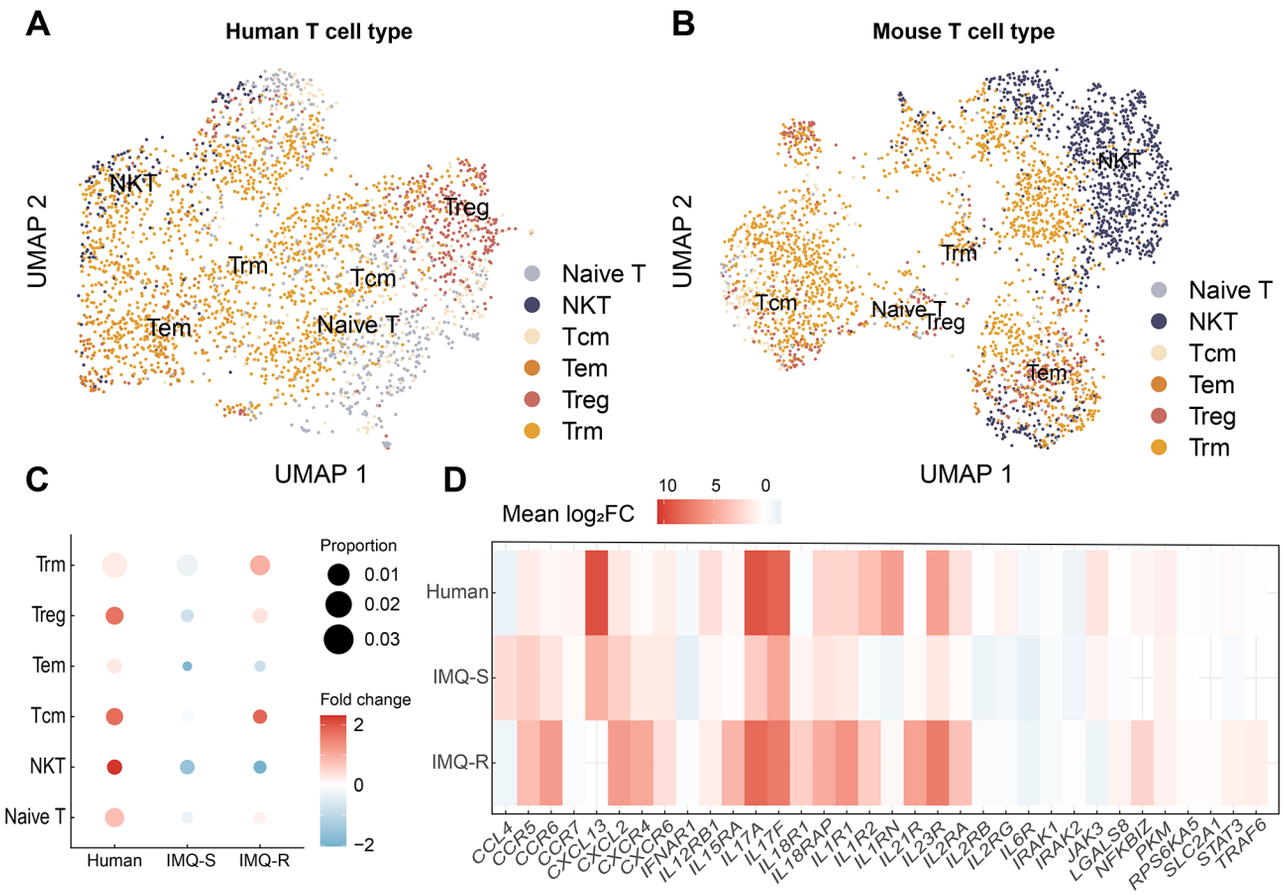


Figure 3 T-cell subsets in skin tissues from psoriasis patients, IMQ-S, and IMQ-R mouse models

A, B: UMAP projections of T cells from psoriasis patients (A) and from IMQ-S and IMQ-R mouse models (B), colored by T-cell subtype. C: Heatmap showing changes in the proportions of T-cell subsets in psoriasis patients, IMQ-S, and IMQ-R relative to their respective controls. Circle size represents the proportion of each subset within total T cells in the patient (model) group, and color indicates fold change compared with controls. D: Fold changes in the average expression of psoriasis-associated key genes in T cells from psoriasis patients, IMQ-S, and IMQ-R relative to their respective control groups (CTL-S, CTL-R). CTL: Control group; IMQ-S: Single-course IMQ model; IMQ-R: Repeated IMQ-challenge model.

Pseudotime trajectory analysis delineates keratinocyte state transitions and transcriptional programs in human psoriasis and IMQ mouse models

To characterize KC state transitions under inflammatory and stress conditions in human psoriatic lesions and IMQ-induced mouse models, we performed pseudotime trajectory analysis based on scRNA-seq data. This approach reconstructs a continuous cellular progression along an inferred temporal axis, enabling inference of dynamic differentiation pathways and transcriptional programs in the absence of true longitudinal sampling. In human and mouse skin, KCs followed a continuous differentiation trajectory that could be partitioned into 10 transcriptionally distinct states (Supplementary Figure S15A–C). These states were distributed in a stage-specific manner along pseudotime, reflecting a gradual progression from basal homeostasis through stress adaptation and inflammatory activation to terminal differentiation.

Time-resolved analysis identified three major transcriptional patterns in human skin (Supplementary Figure S15D). Pattern 1 was upregulated early, peaking at mid-pseudotime and declining thereafter. It comprised differentiation-associated genes (*CALML5, KRTDAP, SBSN, KRT10,* and *DMKN*) and was enriched for cornified envelope formation, estrogen signaling, and fatty acid elongation, consistent with early commitment to terminal differentiation and barrier formation. Pattern 2 remained low at early pseudotime but rose sharply later, containing *GSN, MPZ, PMP22, CD74, IGFBP7, VIM,* and *ACTA2* along with multiple HLA class II molecules; enrichment for hematopoietic cell lineage, asthma, and intestinal immune network for IgA production suggested acquisition of immune-interactive features and transition toward an immunologically active KC phenotype. Pattern 3 showed high expression at early pseudotime followed by a progressive decline. It included *DCN, CFD,* and *FTH1*, and was associated with gene sets annotated with Coronavirus disease–COVID-19, proteoglycans in cancer, and cornified envelope pathways, indicating early stress adaptation and extracellular matrix remodeling preceding stabilization of the epidermal response.

Comparative analysis revealed distinct KC dynamics in IMQ models. In IMQ-S, two transcriptional patterns were observed (Supplementary Figure S15E). Pattern 1 showed minimal expression at early pseudotime but strong induction at later stages, encompassing differentiation keratins (*Krt5, Krt1, Krt79, Krtdap, Calm4, Sbsn*), cell-cycle regulators (*Stmn1, Hmgb2, Ube2c*), smooth muscle–related genes (*Acta2, Tagln, Myh11, Myl9, Tpm2*), and antigen-presentation genes (*Cd74, H2-Ab1, H2-Aa*). Functional enrichment pointed to cornified envelope formation, *Staphylococcus aureus infection*, and *Th1/Th2 differentiation*, indicating a highly synchronized, abrupt activation of barrier remodeling and immune programs.

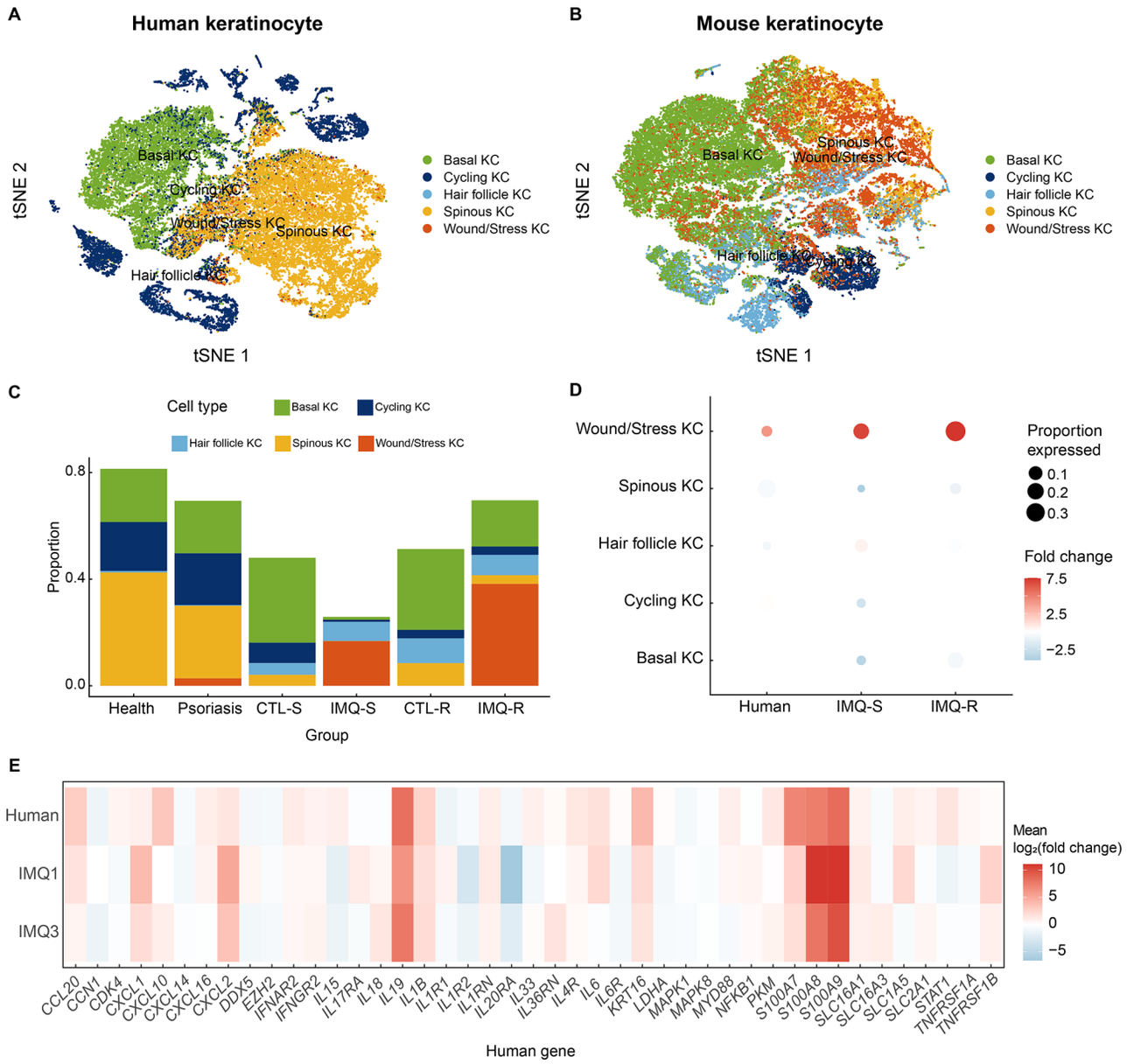


Figure 4 Keratinocyte subtypes in skin tissues from psoriasis patients, IMQ-S, and IMQ-R mouse models

A, B: tSNE projections of keratinocytes from psoriasis patients (A) and from IMQ-S and IMQ-R mouse models (B), colored by keratinocyte subtype. C: Stacked bar charts showing the proportions of keratinocyte subtypes among total cells in psoriasis patients, IMQ-S, IMQ-R, and their respective control groups. D: Heatmap illustrating changes in the proportions of keratinocyte subtypes in psoriasis patients, IMQ-S, and IMQ-R relative to their corresponding controls. Circle size represents the proportion of each subtype within total cells of the patient (model) group, and color indicates fold change compared with controls. E: Heatmap showing changes in the average expression of psoriasis-relevant genes of interest in keratinocytes from psoriasis patients, IMQ-S mouse models, and IMQ-R mouse models. CTL: Control group; IMQ-S: Single-course IMQ model; IMQ-R: Repeated IMQ-challenge model.

Pattern 2 displayed high expression early in pseudotime followed by decline and stabilization, with enrichment for infection-, cytokine-, and cornification-related pathways, reflecting a stress-dominated rather than progressively differentiated response.

In IMQ-R, two transcriptional programs were also identified (Supplementary Figure S15F), but their kinetics more closely resembled those observed in human trajectories. Pattern 1 increased early and then gradually decreased, enriched for *Coronavirus disease–COVID-19*, *arrhythmogenic right ventricular cardiomyopathy*, and *cornified envelope formation*, consistent with a reversible early stress-response phase. Pattern 2 remained stable at early pseudotime but was strongly induced at later stages. This pattern incorporated antigen-presentation genes (*H2-Eb1, H2-Aa, H2-Ab1, Cd74*), inflammatory mediators (*Il18*), differentiation genes (*Krt23, Sbsn, Calm4, Krtdap*), and terminal cornified envelope components (*Flg2* and *Lce1* family members). Enrichment for *cornified envelope formation*, *Staphylococcus aureus infection*, and *rheumatoid arthritis* indicated sustained inflammatory signaling tightly coupled to terminal differentiation.

Collectively, integration of pseudotime trajectories and transcriptional programs demonstrates that IMQ-R more faithfully recapitulates the dynamic progression of human KCs—from early stress responses to a state in which

persistent inflammatory signaling coexists with terminal differentiation—whereas IMQ-S represents a more abrupt and partially dysregulated activation lacking the gradual, stage-resolved evolution observed in human psoriasis.

IMQ-R preferentially enhances neutrophil and tissue-resident macrophage-associated responses and promotes IL-17–associated tissue inflammation compared with IMQ-S

To compare how IMQ-S and IMQ-R shape myeloid-cell composition and inflammatory features, we analyzed cutaneous myeloid populations. A total of 40 080 cells were included, comprising NS (173), PP (1 335), CTL-S (6 264), IMQ-S (11 490), CTL-R (17 004), and IMQ-R (3 814). For populations absent or nearly absent in controls, a minimal pseudocount was applied when calculating fold changes to avoid artefactual inflation and ensure robust comparisons. Automated annotation combined with canonical transcriptional signatures classified myeloid cells into cDCs, pDCs, cycling macrophages, resident macrophages, monocytes, and neutrophils (Figure 5A, B; Supplementary Figures S16, S17), allowing discrimination of recruitment-, residency-, and differentiation-related states. Proportional and fold-change analyses (PP vs. NS, IMQ-S vs. CTL-S, IMQ-R vs. CTL-R; Figure 5C, D) showed that PP lesions exhibited the strongest neutrophil expansion, from near absence in NS, accompanied

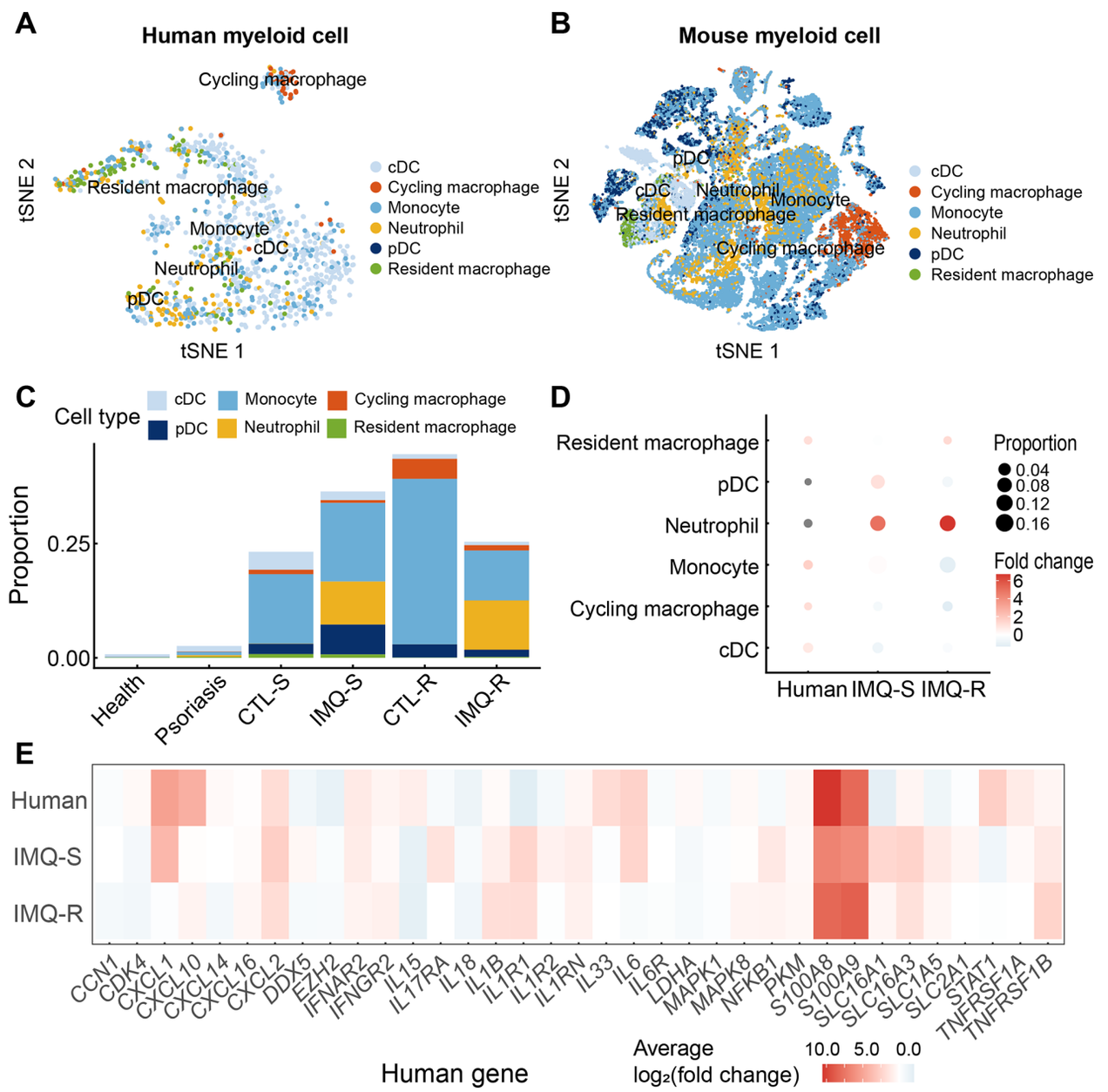


Figure 5 Myeloid cell subtypes in skin tissues from psoriasis patients, IMQ-S, and IMQ-R mouse models

A, B: tSNE projections of myeloid cells from psoriasis patients (A), the IMQ-S and IMQ-R models (B), colored by cell type. C: Stacked bar charts showing the proportions of myeloid subtypes among total cells in psoriasis patients, IMQ-S, IMQ-R, and their respective control groups. D: Heatmap illustrating changes in the proportions of myeloid subtypes in psoriasis patients, IMQ-S, and IMQ-R relative to their corresponding controls; circle size represents the proportion of each subtype within total cells of the patient/model group, and color indicates fold change compared with controls. E: Heatmap showing the average expression changes of psoriasis-relevant pathway genes of interest in myeloid cells across psoriasis patients, the IMQ-S mouse model, and the IMQ-R mouse model. CTL: Control group; IMQ-S: Single-course IMQ model; IMQ-R: Repeated IMQ-challenge model.

by cycling macrophages (3.14-fold) and resident macrophages (2.90-fold), reflecting pronounced innate immune activation.

Compared with IMQ-S, IMQ-R induced substantially greater expansion of neutrophils (141.27-fold vs. 822.75-fold) and resident macrophages (2.90-fold vs. 3.61-fold), while cycling macrophages were reduced, indicating that IMQ-R favors activation and functional specialization of tissue-resident myeloid populations, rather than predominantly promoting proliferative or recruitment-driven macrophage responses. To assess inflammatory programming, we examined a literature-derived psoriasis-associated gene set encompassing chemokines (e.g., *CXCL1, CXCL2*), cytokine signaling (e.g., *IL1B, IL1R1, IL1RN, IL33*), antimicrobial amplifiers (e.g., *S100A8, S100A9*), metabolic/stress genes (e.g., *LDHA, SLC16A1, SLC16A3*), and NF-κB components (e.g., *NFKB1, MAPK1, MAPK8*). Despite stronger neutrophil expansion in IMQ-R, genes linked to acute recruitment and rapid inflammatory amplification (e.g., *CXCL1, CXCL2, IL6, IL17RA, and SLC16A1*) were less upregulated than in IMQ-S. Instead, IMQ-R exhibited higher expression of cytokine-integration genes such as *IL1B* and *TNFRSF1B*, indicating a shift toward a cytokine-structured inflammatory environment that is permissive for sustained interactions among myeloid cells, keratinocytes, and other immune populations.

We next compared the capacity of IMQ-S and IMQ-R to induce TRM-related transcriptional programs. Relative to IMQ-S, IMQ-R showed clear enrichment of a TRM17-like signature, marked by elevated expression of IL-17 effector genes (*Il17a, Il17f*) and an increase in TRM17-like features. IMQ-R also upregulated molecules linked to tissue residency and lipid metabolic adaptation, including *Fabp5* and *Itgae* (CD103), indicating acquisition of skin-resident-associated features. Genes associated with memory maintenance and homeostatic responsiveness (*Il7r* and *Ikzf3*) were likewise higher, supporting a T-cell state with memory-related features. *Cd69* was interpreted cautiously in this analysis since it can reflect both tissue residency and recent activation. Thus, *Cd69* was not used as an independent residency marker, and the TRM17-like interpretation was based on the combined pattern of *Il17a/Il17f, Itgae, Fabp5, Il7r, Ikzf3*, and related markers rather than *Cd69* alone. Stronger *Cd69* induction in IMQ-S therefore may be compatible with an activated T-cell state, but not sufficient by itself to distinguish activation from residency. In contrast, IMQ-R preferentially enriched core TRM17-related genes without parallel upregulation of pan-activation markers such as *Cd3e*, indicating a TRM17-like IL-17-producing transcriptional profile (Supplementary Figure S18A).

At the keratinocyte level, IMQ-R was predicted to elicit a stronger IL-17–associated epidermal response than IMQ-S. IL-36 family members (*Il36a, Il36b* and *Il36g*) were significantly increased, with *Il36g* showing the most pronounced expansion. As key IL-1–family inflammatory amplifiers implicated in psoriasis, IL-36 cytokines can be induced by IL-17 in KCs and, in turn, enhance IL-17–producing T-cell activation. Consistently, *Ccl20* expression was higher in IMQ-R, compatible with enhanced recruitment and positioning of $CCR6^+$ Th17/TRM17 cells. *Tnf* was only modestly elevated, suggesting that IMQ-R favors psoriasis-specific IL-17–IL-36 signaling rather than generalized inflammatory activation (Supplementary Figure S18B).

At the myeloid level, IMQ-R showed higher expression of *Il12b, Il1b, and Tnf*, together with increased frequencies of activated myeloid populations. Despite limited changes in *Il23a*, elevated *Il12b* may imply greater functional availability of IL-23 to sustain Th17/TRM17 activity. In contrast, *Il6* was relatively higher in IMQ-S, reflecting a more acute inflammatory milieu, whereas IMQ-R established a cytokine environment consistent with IL-17-associated chronic inflammation (Supplementary Figure S18C).

Consistent with these transcriptomic and cellular interaction analyses, immunohistochemical staining revealed significantly higher abundance of the T-cell marker CD3 and the residency-associated marker CD103 in IMQ-R lesions compared with IMQ-S (Figure 6A–C). Given that CD3 and CD103 were detected by separate IHC staining rather than multiplex co-localization, this result was interpreted as marker-level support for increased TRM-related signals. To further validate the resident memory like-T17 related phenotype at the functional level, we performed flow cytometric analysis of mouse skin single-cell suspensions following *ex vivo* stimulation and intracellular cytokine staining. Given previous studies have linked reappearing psoriatic lesions to IL-17A-producing $CD8^+CD103^+$ TRM cells in the epidermis (Kurihara et al., 2019), we further assessed the $CD8^+$ TRM17-like subset in addition to the total resident memory like T17 population. Flow cytometric analysis of mouse skin single-cell suspensions following ex vivo stimulation and intracellular cytokine staining also showed a significantly increased proportion of $CD45^+CD3^+CD69^+CD103^+IL\text{-}17A^+$ resident memory like T17 cells in IMQ-R compared with CTL or IMQ-S (Figure 6D–F; IMQ-S vs. IMQ-R, resident memory-like T17 cells/T cells, 0.700±0.429% vs 3.198±0.749%, P<0.0001; resident memory-like T17 cells/TRM-like cells, 2.053±1.183% vs 9.847±2.026%, P<0.0001). Importantly, since this analysis was performed within the $CD3^+$ T-cell gate, it also addressed the possibility that CD103 expression detected in tissue sections could derive from non-T-cell populations. We further found that the $CD8^+$ TRM17-like subset was markedly enriched in IMQ-R relative to IMQ-S (Figure 6G–I; IMQ-S vs. IMQ-R, $CD8^+$ TRM17-like cells/$CD8^+$ T cells, 0.800±0.293% vs. 3.685±0.938%, P<0.0001; $CD8^+$ TRM17-like cells/$CD8^+$ TRM-like cells, 1.907±0.649% vs. 8.642±2.198%, P<0.0001). As an additional relative-abundance measure, these populations were normalized to per million live cells in the digested epidermal cell suspension, which again showed enrichment of resident memory-like T17 cells and $CD8^+$ TRM17-like cells in IMQ-R (Supplementary Figure S19). This normalization does not replace absolute quantification per unit area of lesional skin, but it helps evaluate relative enrichment within viable skin-derived cells under matched processing conditions. Notably, the overall proportion of $CD69^+CD103^+$ TRM-like cells within total skin T cells did not show a corresponding increase in IMQ-R and may be affected by expansion of the total inflammatory T-cell pool under challenge conditions (Supplementary Figure S20). These findings suggest that repeated IMQ challenge preferentially promotes pathogenic IL-17A-producing skewing within the skin TRM-like T cells compartment, particularly in $CD8^+$ cells, rather than indiscriminate expansion of all TRM-like cells. Moreover, flow cytometric analysis demonstrated a marked increase in memory precursor T cells ($IL\text{-}7R^+KLRG1^-$) in the spleen of IMQ-R-treated mice, providing independent tissue-level and systemic evidence that IMQ-R may promote the establishment and maintenance of immune memory (Figure S21A–D).

Collectively, these results indicate that IMQ-R is associated with coordinated multicellular inflammatory programs involving

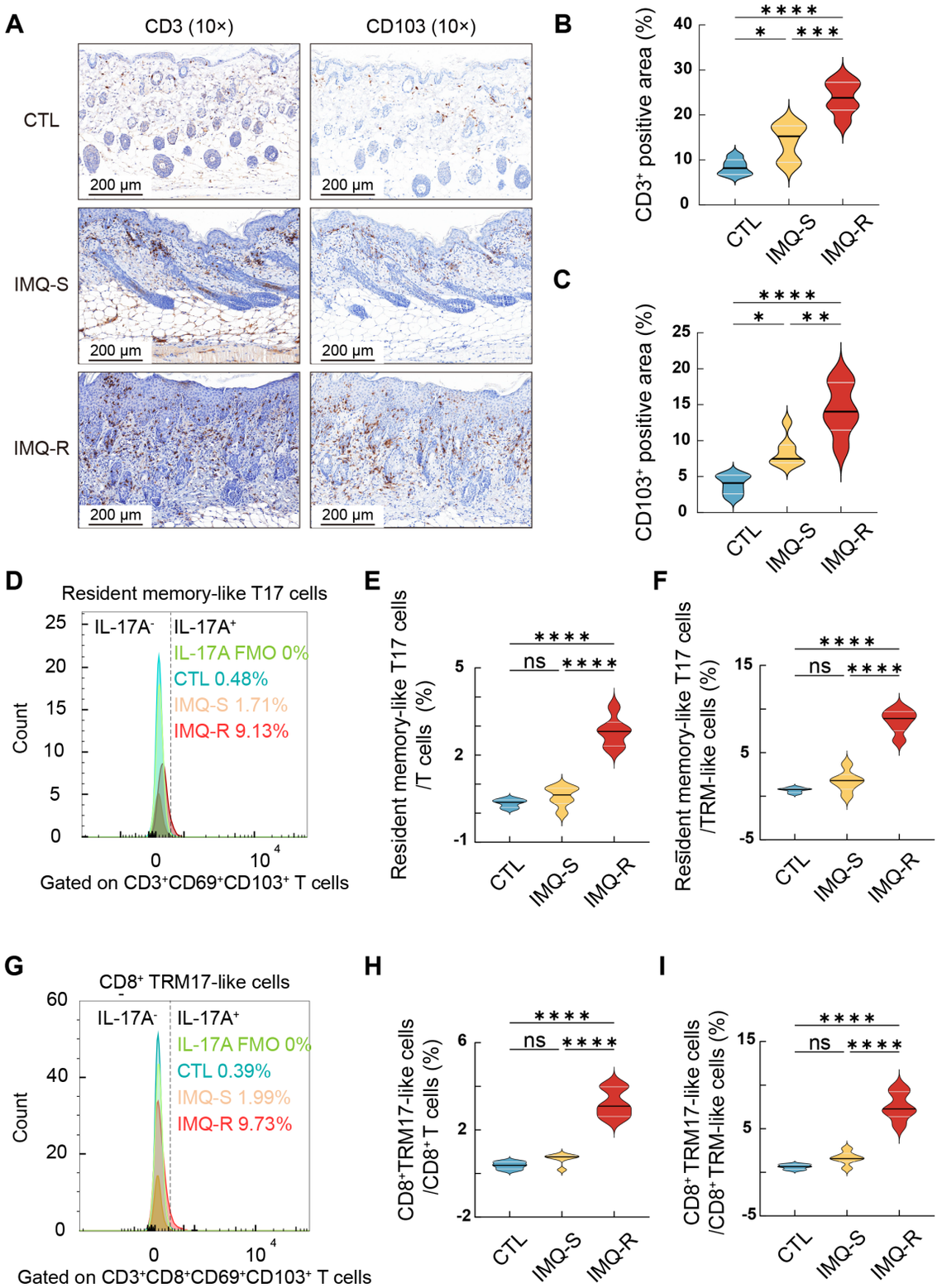


Figure 6 Increased TRM-related marker abundance and IL-17A-producing resident memory-like T-cell populations in IMQ-R skin lesions

A: Representative immunohistochemical staining of CD3 and CD103 in dorsal skin lesions from CTL, IMQ-S, and IMQ-R mice. CD3 and CD103 were stained on separate tissue sections and were used as TRM-related marker-level evidence. Scale bars: 200 μm. B, C: Quantification of $CD3^+$ positive area B: and $CD103^+$ positive area C: in skin lesions from CTL, IMQ-S, and IMQ-R mice. D: Representative histogram showing IL-17A staining in resident memory-like T17 cells, defined as $CD3^+CD69^+CD103^+IL\text{-}17A^+$ cells after gating on epidermal $CD45^+CD3^+$ T cells. The IL-17A FMO control was used to determine the $IL\text{-}17A^+$ gate. E, F: Quantification of resident memory-like T17 cells as a percentage of total T cells (E) and TRM-like cells (F). G: Representative histogram showing IL-17A staining in $CD8^+$ TRM17-like cells, defined as $CD3^+CD8^+CD69^+CD103^+IL\text{-}17A^+$ cells after gating on epidermal $CD45^+CD3^+CD8^+$ T cells. H, I: Quantification of $CD8^+$ TRM17-like cells as a percentage of $CD8^+$ T cells (H) and $CD8^+$ TRM-like cells (I). Violin plots summarize the distribution of values across biological replicates. ns: Not significant; *: $P<0.05$; **: $P<0.01$; ***: $P<0.001$; ****: $P<0.0001$.

keratinocyte IL-17-responsive pathways, myeloid cytokine support, and preferential expansion of neutrophils and resident macrophage-like populations. Although the enrichment of IL-17-associated resident memory-like T-cell features during re-exposure is supported, the precise cellular source of IL-17A and its causal contribution still require further phenotyping and functional validation.

Comparative CellChat analysis suggests altered intercellular communication patterns in IMQ-R during inflammatory re-exposure

Re-emergence of psoriatic inflammation has been associated with sustained interactions of multiple cell types within the local cutaneous immune microenvironment, particularly crosstalk among KCs, dendritic cells (DCs), and T cells (Sieminska et al., 2024; Swindell et al., 2013). To evaluate how well IMQ-S and IMQ-R represent these multicellular inflammatory interactions during the final inflammatory phase, we applied the CellChat framework to compare cell–cell communication networks in both models. Globally, IMQ-R showed a greater increase than IMQ-S in both the number and strength of inferred intercellular interactions. Relative to their respective controls, the total number of communications increased by approximately 1.15-fold in IMQ-S versus CTL-S and by 1.59-fold in IMQ-R versus CTL-R (Figure S22A), indicating a denser interaction network. In contrast, mean interaction strength slightly declined in IMQ-S (~0.93-fold vs. CTL-S), whereas IMQ-R exhibited a marked increase (~1.50-fold vs. CTL-R; Figure S22B), suggesting enhanced potential for intercellular signaling.

Given the enrichment of TRM-like annotations and TRM17-related transcriptional features in IMQ-R, we next examined signaling involving TRM-like subsets. In IMQ-S, the TRM-like subset mainly enhanced outward *CXCL* chemotactic signals, consistent with acute immune recruitment. By contrast, the TRM-like subset in IMQ-R displayed more complex communication patterns, characterized by increased outbound *IL-17* and *CXCL* signaling, greater inbound CCL input, and bidirectional activation of the KLK pathway (Figure S22C, D). Network-level analysis across myeloid cells, KCs, and T cells showed that IMQ-S was dominated by pathways typically associated with acute inflammation, including *IFN-II*, *IL-6*, *IL-17*, *COMPLEMENT*, and *TWEAK*, together with strong chemokine-driven recruitment signals (*CXCL*, *ANGPT*, *ANGPTL*, *VEGI*, *NPR2*). In addition, signaling linked to stress/injury and dysregulated repair (*ANNEXIN*, *VISFATIN*, *SPP1*, *PLAU*; *TGFβ*, *ACTIVIN*, *GDF*, *FGF*, *PDGF*, *NRG*, *PERIOSTIN*) was prominent (Figure S23A, B). This pattern is more suggestive of an acutely inflamed and dynamically recruited network than of a stable tissue-resident niche.

In contrast, IMQ-R was enriched for programs consistent with a tissue-resident-associated inflammatory niche. Persistently active IL-17-centered signaling cooperated with IL-1 and TWEAK pathways, while integrin/ECM-associated axes (*PERIOSTIN*, *ANGPTL*, *PLAU*, *SEMA3*, *SLIT*) suggested enhanced spatial anchoring. Pathways related to metabolism-immune coupling and homeostatic regulation (*VISFATIN*, *RBP4*, *ENHO*, *TULP*) were also enriched, alongside GAS6-AXL-related tolerance and survival signals (*GAS*, *BAFF*, *RANKL*), which have been implicated in immune persistence. These occurred together with more regulated chemokine signaling (*CCL*, *CXCL*, *CX3C*) and controlled remodeling pathways (*PDGF*, *NRG*, *BMP*, *TGFβ*, *MK*, *KLK*) that have previously been reported as features in human psoriasis (Figure S23C, D). Ligand-receptor probability analysis further suggested selectively enhanced IL-17 signaling from TRM-like cells to wound/stress-associated KCs in IMQ-R, an interaction that was less evident in IMQ-S (Figure S24; Supplementary Table S3). These results suggest the presence of an enhanced IL-17 inflammatory interaction module between TRM-like cells and KCs in the repeated-challenge model.

Overall, these data suggest that IMQ-R may better approximate the complexity and organization of intercellular communication in psoriasis than IMQ-S, with TRM-related T cells emerging as a prominent predicted signaling node within the cutaneous inflammatory network.

DISCUSSION

Recent reevaluations have highlighted important limitations of the conventional IMQ model as a surrogate for human psoriasis, especially when questions of chronicity and lesion reactivation are being addressed (Smith et al., 2026). While IMQ robustly induces epidermal hyperplasia and activation of the IL-23/IL-17 axis, it primarily reflects an acute, TLR7-driven innate inflammatory response rather than the sustained, site-restricted immune state observed in patients. Repeated IMQ protocols have therefore been explored as an attempt to introduce prior inflammatory exposure and tissue-level adaptations into this experimental system. In our study, the IMQ-R design incorporated repeated induction cycles separated by visible recovery intervals, allowing us to compare a previously challenged skin environment with a single-course acute response. This design is useful for studying inflammatory reactivation after repeated challenge and associated tissue adaptations.

Re-emergence of psoriatic lesions is increasingly understood as a multicellular process sustained by reciprocal signaling among epithelial, stromal, and adaptive immune compartments rather than a transient cytokine burst (Sieminska et al., 2024; Yao et al., 2025). Within this framework, our single-cell data suggest that the IMQ-S and IMQ-R models represent distinct inflammatory states. In IMQ-S, cellular composition is dominated by a marked expansion of myeloid populations with comparatively limited T-cell engagement, consistent with prior single-cell studies showing that the classical IMQ model primarily mirrors an acute innate inflammatory reaction rather than adaptive immune memory formation (Jin et al., 2022; Qie et al., 2020). In IMQ-R, the cellular landscape includes KC expansion, EC enrichment, and preserved T-cell representation, producing a cellular architecture that overlapped more extensively with human psoriasis, indicating that repeated challenge shifts the model toward a tissue context more compatible with inflammatory reactivation after prior exposure. Although the IMQ-R model was not able to fully recapitulate all aspects of human disease, this distinction supports the use of IMQ-R for investigating TRM-related tissue programs and repeated-challenge inflammatory organization, whereas IMQ-S may remain more suitable for studying acute innate inflammatory responses, early chemokine induction, and rapid epidermal stress reactions.

Inter-individual variation in cell recovery and fluctuations in cellular composition may influence the interpretation of changes in major cell populations and T-cell subclusters across the two mouse models. In particular, estimates of rare immune subsets can be affected by limited sample size and

uneven cell capture, and future studies with larger numbers of biological replicates and deeper single-cell profiling would help provide a more stable assessment of these population-level changes. Based on the currently available data, we therefore performed equal-cell-number downsampling and leave-one-sample-out sensitivity analyses to evaluate the robustness of the observed trends. In these analyses, the increases in several major cell populations, including endothelial cells, keratinocytes, and T cells, remained consistently greater in the IMQ-R model than in the IMQ-S model when each model was compared with its corresponding control. Similarly, within the T-cell compartment, the proportional changes of TRM-like and TCM-like subpopulations were also more pronounced in the IMQ-R model than in the IMQ-S model. These findings suggest that, although the compositional analyses should be interpreted with appropriate caution, the main trends observed in the IMQ-R model were not solely driven by unequal cell recovery or by any single individual sample.

Our cell-cell communication analysis further supports the idea that repeated challenge reshapes the local inflammatory niche. Previous work on IMQ-induced inflammation has shown that although overall intercellular communication may be reduced compared with normal skin, specific activated populations—particularly inflammatory fibroblasts and EMT-like keratinocytes—can acquire disproportionate signaling influence and function as dominant communication hubs (Guo et al., 2024). Our findings extend this observation by showing enhanced predicted communication between TRM—like cells and stress-responsive KCs after repeated IMQ challenge. This strengthened TRM-KC interaction is consistent with a localized communication pattern that may facilitate faster inflammatory reactivation after restimulation. However, as these results are derived from CellChat-based inference rather than direct functional testing, subsequent experimental validation is still needed to confirm their biological relevance.

Clinical and translational studies have shown that even after apparent resolution of psoriatic lesions, IL-17A-producing αβ T-cell clones remain detectable in previously affected skin, where their IL-17A production is substantially higher than in healthy skin (Blauvelt & Chiricozzi, 2018) . In addition, IL-17A/F double-positive T cells, destabilized Tregs, and quiescent TRM populations have been implicated in inflammation after treatment withdrawal (Matos et al., 2017; Peng et al., 2024; Puig et al., 2022) . Against this background, our data indicate that IMQ-S and IMQ-R differ not only in the extent of IL-17-related activation but also in the quality of the associated T-cell program. Consistent with prior reports (Swindell et al., 2017), the IMQ-S model showed increased expression of *Il17a, Il17b, Il17c*, and *Il17f* in T cells; however, transcriptional programming of *Il23r, Ccr6, Il7r*, and *Il17r* remained limited, suggesting limited induction of this T-cell program. By contrast, IMQ-R exhibited enhanced TRM17-related transcriptional features at both the whole-transcriptome and T-cell-specific levels, including *Il23r, Il21r, Ccr6, Il17a, Il17f, Fabp5*, and *Il7r*. This was accompanied by upregulation of IL-17 pathway-associated genes in keratinocytes and myeloid cells, such as *Il36a, Il36b*, and *Il36g* in keratinocytes and Il12b, Il1b, and *Tnf* in myeloid cells, suggesting coordinated responses across multiple psoriasis-relevant immune and parenchymal compartments during final re-exposure. At the same time, the disease-relevant IL-17-producing compartment in IMQ-induced psoriasiform inflammation may not be restricted to conventional αβ TRM cells, because γδ T cells can serve as major IL-17A-producing effector populations in this model and may display resident or memory-like features in skin (Hartwig et al., 2015). Our use of epidermal single-cell suspensions should reduce the contribution of dermal γδT17 cells, and the additional $CD8^+$ gate further reduces potential contribution from classical epidermal dendritic epidermal T cells and dermal γδT17 cells, which are generally CD4-CD8- rather than conventional $CD8^+$ αβ T cells. However, because TCRβ and TCRγδ were not included in the current flow-cytometry panel, the broader $CD45^+CD3^+CD69^+CD103^+$IL-$17A^+$ population cannot be assigned exclusively to αβ T cells. We therefore refer to this gate as resident memory-like T17 cells and to the CD8-gated population as $CD8^+$ TRM17-like cells. Therefore, the T-cell features enriched in IMQ-R may reflect a broader resident inflammatory compartment in skin rather than only a single narrowly defined αβ TRM subset. As TRM17 cells are difficult to culture and study experimentally, enrichment of these features in IMQ-R may make this model useful for mechanistic studies of repeated-challenge IL-17-associated skin inflammation.

These molecular and cellular observations were paralleled by organism-level phenotypes. IMQ-R lesions displayed a more rapid inflammatory response upon re-challenge, together with increased abundance of CD3 and CD103 staining in tissue sections and enrichment of IL-17A-producing resident memory-like T cells by flow cytometry. Notably, the overall proportion of $CD69^+CD103^+$ cells within epidermal skin T cells did not increase uniformly in IMQ-R and may have been influenced by expansion of the total inflammatory T-cell pool under challenge conditions. In contrast, the IL-17A-producing fraction within the resident memory-like compartment was markedly increased in IMQ-R, indicating preferential pathogenic skewing rather than a simple numerical expansion of all TRM-like cells. Splenic analysis also showed expansion of memory precursor-associated populations. Together, these findings suggest that IMQ-R is distinguished less by the absolute magnitude of inflammation than by the speed of the cutaneous response and the enrichment of TRM-related, IL-17-skewed features upon re-challenge (Lin et al., 2026).

Collectively, our results indicate that the purpose of the IMQ-R protocol is not simply to generate stronger or more prolonged inflammation, but to provide a controlled re-exposure setting for examining features that emerge when previously inflamed skin is challenged again. Rather than indicating a fully defined shift to a TRM17-driven process, the data suggest that repeated IMQ challenge is associated with enrichment of IL-23R/CCR6/TRM17-related features and with stronger tissue programs relevant to inflammatory reactivation. In this sense, IMQ-R may provide a useful experimental framework for studying repeated-challenge psoriasiform inflammation and for testing interventions aimed at interrupting local type 17 inflammatory circuits, while not fully capturing the entire clinical course of psoriasis relapse (Puig et al., 2022).

Since IMQ is a pharmacologic TLR7/8 agonist, the accelerated response in IMQ-R should not be interpreted as direct evidence of antigen-specific adaptive recall or as a process driven exclusively by TRM-like cells. Repeated topical stimulation may enhance inflammation through several non-mutually exclusive mechanisms, including primed innate myeloid responses, KC or epidermal stem-cell inflammatory memory, altered TLR responsiveness, persistent IL-23/IL-17/IL-36-related cytokine circuits, cumulative tissue

remodeling, stromal or fibroblast inflammatory imprinting, and vascular or neuroimmune remodeling. Psoriasis also lacks a single defined exogenous antigen comparable to infectious disease models. Instead, multiple self-derived or tissue-associated candidate antigens have been reported, including LL37, ADAMTSL5, PLA2G4D-derived neolipid antigens, and keratin 17, suggesting that antigen-reactive T-cell responses may differ across patients and may coexist within the same individual. Thus, the current study evaluates total resident memory-like T17 and $CD8^+$ TRM17-like populations rather than psoriasis-antigen-specific TRM cells.

From a translational perspective, the TRM17-related programs highlighted in IMQ-R point to several therapeutic axes of interest. Current biologics targeting the IL-23/IL-17 pathway provide the strongest evidence that interrupting pathogenic type 17 immune programs can improve psoriasis and may influence persistent inflammatory programs in previously affected skin (Blauvelt et al., 2025; Puig et al., 2022; Vu et al., 2021). In parallel, the CCL20–CCR6 axis remains a plausible target for limiting the positioning or recruitment of pathogenic T17/TRM-related cells in skin(Guo et al., 2023; Shi et al., 2023), whereas tissue-retention pathways involving CD103–E-cadherin represent a mechanistically relevant, although still largely preclinical, direction (Kasprowicz-Furmańczyk et al., 2021). More broadly, peptide-based therapeutics have increasingly been recognized as a promising skin-targeted strategy for their potential to modulate protein–protein interactions, inflammatory signaling, and local tissue repair, with emerging evidence from animal-derived peptides showing anti-inflammatory and immunomodulatory activities that may be relevant to local tissue disease control (Fu et al., 2026; Li et al., 2026; Liao et al., 2026; Liu et al., 2026; Ru et al., 2025; Wang et al., 2025; Wu et al., 2024). These considerations further raise the possibility that peptide-based approaches may be adaptable to psoriasis reactivation biology, as bioactive peptides derived from animal secretions have shown diverse pharmacologic and immunomodulatory properties that could, in principle, be harnessed to target IL-17-related signaling, interfere with CCL20–CCR6-guided positioning of pathogenic T17/TRM-related cells, or disrupt tissue-retention interactions such as CD103–E-cadherin (Lai et al., 2026). Although these strategies remain largely conceptual in psoriasis, recent work on animal-derived bioactive peptides supports the broader idea that future long-term disease-control approaches may need not only to suppress active inflammation, but also to reshape the pathogenic tissue microenvironment and persistent inflammatory compartment that remain in previously affected skin (Deng et al., 2024b; Lai et al., 2026; Liao et al., 2026; Vu et al., 2021).

Several limitations should be acknowledged. First, although the repeated IMQ protocol captures accelerated inflammatory re-emergence and selected TRM-related features, it remains a pharmacologic TLR7-driven model. More recent mechanistic work further supports this view by showing that ANKRD22 promotes resolution of psoriasiform inflammation through antagonism of NIK-mediated IL-23 production, highlighting active host mechanisms that limit sustained inflammation in this setting (Xia et al., 2024). Accordingly, the faster response observed in IMQ-R may be compatible with tissue adaptation after repeated inflammatory challenge, but it does not by itself identify the responsible cell type or demonstrate antigen-specific adaptive immune memory. We focused on the final induction phase, as it most directly captures the active inflammatory cascade that emerges when previously challenged skin is re-exposed to stimulus. Human lesional skin was chosen as the comparator for this active inflammatory phase, whereas comparison with clinically resolved human skin would be highly informative for future studies of remission-phase or previously affected tissue states. Gross observations across the induction and remission phases further showed that visible lesions largely resolved during the interval periods before the final re-challenge, although the extent to which remission-phase murine skin reproduces clinically resolved human lesions remains to be further defined. Second, most analyses in the present study were performed during the final induction phase; although supplementary images support visible resolution during the remission intervals, remission-phase skin was not profiled at the same molecular depth as the final lesions. Therefore, the current data do not directly define a remission-phase tissue-memory state. Third, the number of T cells captured in the scRNA-seq dataset was limited, leaving relatively few cells for downstream T-cell analysis. In comparable whole-skin IMQ mouse scRNA-seq studies without prior immune-cell enrichment, recovered T-cell numbers have likewise been modest; for example, one study detected 625 T cells in total (Qie et al., 2020). Under these conditions, limited T-cell numbers may constrain downstream analyses by reducing the resolution of T-cell subset annotation, making rare subsets more difficult to identify reliably, increasing variability in estimated subset abundance, and weakening the robustness of T cell-focused differential expression and interaction analyses. For this reason, TRM17-related changes in the present study were further assessed by flow cytometry and immunohistochemistry rather than relying solely on scRNA-seq-based clustering. Fourth, the flow-cytometry definitions used here should be regarded as working phenotypic definitions. CD69 can reflect both tissue residency and recent activation, and TCRβ/TCRγδ staining was not included; therefore, γδT-derived IL-17A-producing cells cannot be completely excluded, particularly in the broader resident memory-like T17 gate. The $CD8^+$ gate and epidermal suspension strategy reduce this concern but do not replace direct TCR-based phenotyping. In addition, the flow-cytometry results are reported primarily as relative proportions and per-million-live-cell values in digested skin suspensions rather than absolute counts per unit area of lesional skin. Future spatial or bead-based absolute-counting approaches would be needed for direct quantitative enumeration. Fifth, the long-term tissue residency and causal contribution to lesion reactivation of the increased TRM17-like cells in the IMQ-R model remain to be established through lineage-tracing or photoconversion approaches, together with depletion or intervention experiments that directly test their functional requirement; future work may also benefit from more specialized genome-edited immune models for causal validation of candidate pathogenic cell populations (Zheng et al., 2025). Sixth, the TRM17-related networks and IL-17-associated communication patterns presented in this study are correlative and predictive rather than functionally proven causal mechanisms, and the CellChat interactions still have to be validated to confirm the causal role of TRM-like cells and KCs in reactivation. The present study primarily focuses on skin compartments, leaving systemic contributions unexplored. Although overt dose effects were excluded, subtle differences in local IMQ

retention cannot be definitively excluded. Finally, translation to human disease will require validation in patient-derived samples to determine whether the observed TRM-keratinocyte communication networks correspond to previously affected or reactivation-prone human skin. Future studies integrating remission-phase sampling, spatial transcriptomics, antigen-receptor profiling, and interventional perturbation will be important for determining how persistent inflammatory programs are encoded in psoriatic skin and whether disruption of these tissue circuits can prevent lesion re-emergence in IMQ-R and in psoriasis patients, particularly as spatially resolved omics approaches are becoming increasingly informative for dissecting local immune and structural microenvironments in inflamed tissues (Zhao et al., 2026).

DATA AVAILABILITY

The single-cell and bulk RNA-seq transcriptomic dataset supporting the conclusions of this study has been deposited in Science Data Bank (ScienceDB) under DOI: 10.57760/sciencedb.31697 and can be accessed at https://www.scidb.cn/s/yYBZZ3.

SUPPLEMENTARY DATA

Supplementary data to this article can be found online.

COMPETING INTERESTS

The authors declare that they have no competing interests.

AUTHORS' CONTRIBUTIONS

X. T., R. W., C. X. L. and X. M. Z. conceived the study and designed the project, with input from Z. Z. who provided some ideas; X. T. and Z. H. L. performed the *in vivo* and *in vitro* experiment; X. T. and Z. Z. conducted data curation, bioinformatics analysis, visualization; X. T. wrote the manuscript; X. T. and X. M. Z. designed figures; X. M. Z. and R. W. acquired funding and supervised the study; X. T., Z. Z., Z. H. L., C. X. L., R. W. and X. M. Z. provided suggestions for data analysis; C. X. L., R. W. and X. M. Z. revised this manuscript; All authors contributed to data interpretation. All authors read and approved the final version of the manuscript.

ACKNOWLEDGEMENTS

We thank Meng Li (Institute of Zoology, Chinese Academy of Sciences) for the mouse preparation and cellular assay.

REFERENCES

Aran D, Looney AP, Liu LQ, et al. 2019. Reference-based analysis of lung single-cell sequencing reveals a transitional profibrotic macrophage. *Nature Immunology*, **20**(2): 163–172.

Blauvelt A, Chiricozzi A. 2018. The immunologic role of IL-17 in psoriasis and psoriatic arthritis pathogenesis. *Clinical Reviews in Allergy & Immunology*, **55**(3): 379–390.

Blauvelt A, Jiang RD, Shi LY, et al. 2025. A randomized phase 2 clinical trial to treat moderate-to-severe plaque psoriasis patients with high-induction dosing of risankizumab. *Nature Communications*, **17**(1): 733.

Blondel VD, Guillaume JL, Lambiotte R, et al. 2008. Fast unfolding of communities in large networks. *Journal of Statistical Mechanics: Theory and Experiment*, **2008**: P10008.

Cao JY, Spielmann M, Qiu XJ, et al. 2019. The single-cell transcriptional landscape of mammalian organogenesis. *Nature*, **566**(7745): 496–502.

Casciano F, Severi P, Marongiu L, et al. 2025. Highly differentiated T cells link systemic and vascular inflammation in a mouse model of recurrent psoriasis. *Frontiers in Immunology*, **16**: 1574455.

Chen SF. 2023. Ultrafast one-pass FASTQ data preprocessing, quality control, and deduplication using fastp. *iMeta*, **2**(2): e107.

Chen YC, Yan YH, Liu HZ, et al. 2020. Dihydroartemisinin ameliorates psoriatic skin inflammation and its relapse by diminishing $CD8^+$ T-cell memory in wild-type and humanized mice. *Theranostics*, **10**(23): 10466–10482.

Deng GS, Zhang YL, Song JK, et al. 2024a. Liquiritin exerts psoriasis therapy and prevention by regulating the YY1/RBP3 axis. *Phytomedicine*, **134**: 155951.

Deng GS, Zhang YL, Song JK, et al. 2024b. The role and therapeutic strategies for tissue-resident memory T cells, central memory T cells, and effector memory T cells in psoriasis. *Immunology*, **173**(3): 470–480.

Dobin A, Davis CA, Schlesinger F, et al. 2013. STAR: ultrafast universal RNA-seq aligner. *Bioinformatics*, **29**(1): 15–21.

Fenix K, Wijesundara DK, Cowin AJ, et al. 2020. Immunological memory in imiquimod-induced murine model of psoriasiform dermatitis. *International Journal of Molecular Sciences*, **21**(19): 7228.

Francis L, Mccluskey D, Ganier C, et al. 2024. Single-cell analysis of psoriasis resolution demonstrates an inflammatory fibroblast state targeted by IL-23 blockade. *Nature Communications*, **15**(1): 913.

Fu Z, Jiang JY, Jia QY, et al. 2026. The self-assembling amphibian-derived peptide (RADA)4-FZ1 pioneers a novel therapeutic platform for diabetic skin wound management. *Chemical Engineering Journal*, **530**: 173231.

Guo DH, Li XK, Wang J, et al. 2024. Single-cell RNA-seq reveals keratinocyte and fibroblast heterogeneity and their crosstalk via epithelial-mesenchymal transition in psoriasis. *Cell Death & Disease*, **15**(3): 207.

Guo J, Zhang HY, Lin WR, et al. 2023. Signaling pathways and targeted therapies for psoriasis. *Signal Transduction and Targeted Therapy*, **8**(1): 437.

Hartwig T, Pantelyushin S, Croxford AL, et al. 2015. Dermal IL-17-producing γδ T cells establish long-lived memory in the skin. *European Journal of Immunology*, **45**(11): 3022–3033.

Healy J, McInnes L. 2024. Uniform manifold approximation and projection. *Nature Reviews Methods Primers*, **4**(1): 82.

Hu MY, Cao H, Zhang SM, et al. 2025. Interleukin-17A-related inflammation mediates cardiac injury in chronic relapsing psoriasis-like mouse model. *Experimental Dermatology*, **34**(7): e70139.

Jabeen M, Boisgard AS, Danoy A, et al. 2020. Advanced characterization of imiquimod-induced psoriasis-like mouse model. *Pharmaceutics*, **12**(9): 789.

Jin SQ, Plikus MV, Nie Q. 2025. CellChat for systematic analysis of cell–cell communication from single-cell transcriptomics. *Nature Protocols*, **20**(1): 180–219.

Jin SS, Wang YX, Qie CX, et al. 2022. Single-cell RNA sequencing reveals the immune cell profiling in IMQ induced psoriasis-like model. *Journal of Inflammation Research*, **15**: 5999–6012.

Kasprowicz-Furmańczyk M, Czerwińska J, Placek W, et al. 2021. Assessment of the tissue resident memory cells in lesional skin of patients with psoriasis and in healthy skin of healthy volunteers. *International Journal of Environmental Research and Public Health*, **18**(21): 11251.

Kim D, Paggi JM, Park C, et al. 2019. Graph-based genome alignment and genotyping with HISAT2 and HISAT-genotype. *Nature Biotechnology*, **37**(8): 907–915.

Kurihara K, Fujiyama T, Phadungsaksawasdi P, et al. 2019. Significance of IL-17A-producing $CD8^+CD103^+$ skin resident memory T cells in psoriasis lesion and their possible relationship to clinical course. *Journal of Dermatological Science*, **95**(1): 21–27.

Lai SA, Chai JW, Luo YT, et al. 2026. Peptides derived from exocrine secretions of venomous animals used as traditional Chinese "worm" medicines. *Zoological Research*, **47**(1): 233–249.

Li B, Dewey CN. 2011. RSEM: accurate transcript quantification from RNA-Seq data with or without a reference genome. *BMC Bioinformatics*, **12**(1): 323.

Li QY, Pang BY, Dang EL, et al. 2024. Endothelial dysfunction in psoriasis:

an integrative review. *Journal of Investigative Dermatology*, **144**(9): 1935–1942.

Li X, Shao XY, Li XZ, et al. 2025. Novel TNF-α-targeting mRNA therapy for sustained psoriasis treatment and relapse prevention by suppressing IL-15-T_{RM} signaling. *Journal of Controlled Release*, **387**: 114218.

Li YS, Jia QY, Liu NX, et al. 2026. Peptide RL-QN15 regulates functions of epidermal stem cells to accelerate skin wound regeneration via the FZD8/β-Catenin axis. *Exploration*, **6**(3): 20240090.

Liao H, Lai SA, Wang K, et al. 2026. Functional characterization of HR-CATH2, a novel cathelicidin from *Hoplobatrachus rugulosus* with anti-sepsis activity. *Zoological Research*, **47**(3): 785–797.

Lin YK, Chen JY, Du H, et al. 2026. Activation of NF-κB signaling in tissue-resident memory T cells promotes recurrent psoriasis in mice. *Frontiers in Immunology*, **16**: 1762269.

Liu X, Liu J, Li B, et al. 2026. First identification of an amphibian-derived peptide with anti-vascular aging activity. *Zoological Research*, **47**(3): 748–764.

Love MI, Huber W, Anders S. 2014. Moderated estimation of fold change and dispersion for RNA-seq data with DESeq2. *Genome Biology*, **15**(12): 550.

Madsen M, Hansen PR, Nielsen LB, et al. 2018. Imiquimod-induced psoriasis-like skin lesions do not accelerate atherosclerosis in low-density lipoprotein receptor–deficient mice. *The American Journal of Pathology*, **188**(6): 1486–1496.

Masson Regnault M, Shourick J, Jendoubi F, et al. 2022. Time to relapse after discontinuing systemic treatment for psoriasis: a systematic review. *American Journal of Clinical Dermatology*, **23**(4): 433–447.

Matos TR, O'malley JT, Lowry EL, et al. 2017. Clinically resolved psoriatic lesions contain psoriasis-specific IL-17–producing αβ T cell clones. *The Journal of Clinical Investigation*, **127**(11): 4031–4041.

Peng L, Liu WQ, Cheng YF, et al. 2024. IL-17A/F double producing T cells, unstable Tregs and quiescent TRMs in clinically healed lesions are potential cellular candidates for recurrence of psoriasis. *Clinical Immunology*, **266**: 110328.

Pertea M, Pertea GM, Antonescu CM, et al. 2015. StringTie enables improved reconstruction of a transcriptome from RNA-seq reads. *Nature Biotechnology*, **33**(3): 290–295.

Puig L, Costanzo A, Muñoz‐Elías EJ, et al. 2022. The biological basis of disease recurrence in psoriasis: a historical perspective and current models. *British Journal of Dermatology*, **186**(5): 773–781.

Qie CX, Jiang JW, Liu WM, et al. 2020. Single-cell RNA-Seq reveals the transcriptional landscape and heterogeneity of skin macrophages in $Vsir^{-/-}$ murine psoriasis. *Theranostics*, **10**(23): 10483–10497.

Qiu ZH, Huang AL, Li ZH, et al. 2025. Hydrogen-rich water ameliorates imiquimod-induced psoriasis-like skin lesions and regulates macrophage polarization in dyslipidemic ApoE-deficient mice. *European Journal of Pharmacology*, **992**: 177363.

Ritchie ME, Phipson B, Wu D, et al. 2015. *Limma* powers differential expression analyses for RNA-sequencing and microarray studies. *Nucleic Acids Research*, **43**(7): e47.

Ru ZQ, Wu YT, Yang CY, et al. 2025. Ultra-short cyclic peptide $Cy_{RL\text{-}QN15}$ acts as a TLR4 antagonist to expedite oral ulcer healing. *Zoological Research*, **46**(5): 1187–1202.

Rueden CT, Schindelin J, Hiner MC, et al. 2017. ImageJ2: ImageJ for the next generation of scientific image data. *BMC Bioinformatics*, **18**(1): 529.

Saavedra-Almarza J, Malgue F, García-Gómez M, et al. 2025. Unveiling the role of resident memory T cells in psoriasis. *Journal of Leukocyte Biology*, **117**(3): qiae254.

Satija R, Farrell JA, Gennert D, et al. 2015. Spatial reconstruction of single-cell gene expression data. *Nature Biotechnology*, **33**(5): 495–502.

Shi ZR, Mabuchi T, Riutta SJ, et al. 2023. The chemokine, CCL20, and its receptor, CCR6, in the pathogenesis and treatment of psoriasis and psoriatic arthritis. *Journal of Psoriasis and Psoriatic Arthritis*, **8**(3): 107–117.

Sieminska I, Pieniawska M, Grzywa TM. 2024. The immunology of psoriasis—current concepts in pathogenesis. *Clinical Reviews in Allergy & Immunology*, **66**(2): 164–191.

Smith CC, Zwerner IM, Gudjonsson JE, et al. 2026. Reevaluating the imiquimod model: a barrier to translational progress in psoriasis. *Journal of Investigative Dermatology*, **146**(2): 322–327.

Stuart T, Butler A, Hoffman P, et al. 2019. Comprehensive integration of single-cell data. *Cell*, **177**(7): 1888–1902. e21.

Suárez-Fariñas M, Fuentes-Duculan J, Lowes MA, et al. 2011. Resolved psoriasis lesions retain expression of a subset of disease-related genes. *Journal of Investigative Dermatology*, **131**(2): 391–400.

Swindell WR, Johnston A, Voorhees JJ, et al. 2013. Dissecting the psoriasis transcriptome: inflammatory- and cytokine-driven gene expression in lesions from 163 patients. *BMC Genomics*, **14**(1): 527.

Swindell WR, Michaels KA, Sutter AJ, et al. 2017. Imiquimod has strain-dependent effects in mice and does not uniquely model human psoriasis. *Genome Medicine*, **9**(1): 24.

Tian DN, Lai YP. 2022. The relapse of psoriasis: mechanisms and mysteries. *JID Innovations*, **2**(3): 100116.

Tran PTT, Le LT, Le TTV, et al. 2024. Effects of imiquimod application durations on psoriasis-like lesions and cytokine expression in mice. *Biomedical Research and Therapy*, **11**(5): 6387–6401.

Van Der Maaten L, Hinton G. 2008. Visualizing data using t-SNE. *Journal of Machine Learning Research*, **9**(86): 2579–2605.

Vu TT, Koguchi-Yoshioka H, Watanabe R. 2021. Skin-resident memory T cells: pathogenesis and implication for the treatment of psoriasis. *Journal of Clinical Medicine*, **10**(17): 3822.

Wang LT, Fu Z, Su YH, et al. 2025. Cyclic heptapeptide FZ1 acts as an integrin αvβ3 agonist to facilitate diabetic skin wound healing by enhancing angiogenesis. *Journal of Medicinal Chemistry*, **68**(18): 19503–19520.

Wu XK, Zhou HW, Cheng GY, et al. 2025. *Smilax glabra* Roxb. extract alleviates psoriasis-like lesions in mice by the synergistic effects of TOP2A inhibition and AhR activation. *International Immunopharmacology*, **164**: 115408.

Wu YT, Ru ZQ, Peng Y, et al. 2024. Peptide $Cy_{RL\text{-}QN15}$ accelerates hair regeneration in diabetic mice by binding to the Frizzled-7 receptor. *Zoological Research*, **45**(6): 1287–1299.

Xia XC, Zhu LQ, Xu MM, et al. 2024. ANKRD22 promotes resolution of psoriasiform skin inflammation by antagonizing NIK-mediated IL-23 production. *Molecular Therapy*, **32**(5): 1561–1577.

Yao Y, Chen LQ, Lv YB, et al. 2025. Skin immune microenvironment in psoriasis: from bench to bedside. *Frontiers in Immunology*, **16**: 1643418.

Ye JF, Lai YP. 2025. Keratinocytes: new perspectives in inflammatory skin diseases. *Trends in Molecular Medicine*, **31**(12): 1103–1113.

Yu GC, Wang LG, Han YY, et al. 2012. ClusterProfiler: an R package for comparing biological themes among gene clusters. *OMICS: A Journal of Integrative Biology*, **16**(5): 284–287.

Zhang J, Li HY, Tao WJ, et al. 2026. ClusterGVis: an advanced visualization and clustering tool for gene expression analysis. *Genomics, Proteomics & Bioinformatics*, **24**(2): qzag005.

Zhao ZJ, Chen JM, Chen D, et al. 2026. Spatial transcriptomics and N-glycoproteomics reveal breed-dependent immune and structural responses in *Mycoplasma hyopneumoniae*-infected pig lungs. *Zoological Research*, doi: 10.24272/j.issn.2095-8137.2025.612.

Zheng GXY, Terry JM, Belgrader P, et al. 2017. Massively parallel digital transcriptional profiling of single cells. *Nature Communications*, **8**: 14049.

Zheng X, Huang CH, Yan S, et al. 2025. Advances and applications of genome-edited animal models for severe combined immunodeficiency. *Zoological Research*, **46**(1): 249–260.